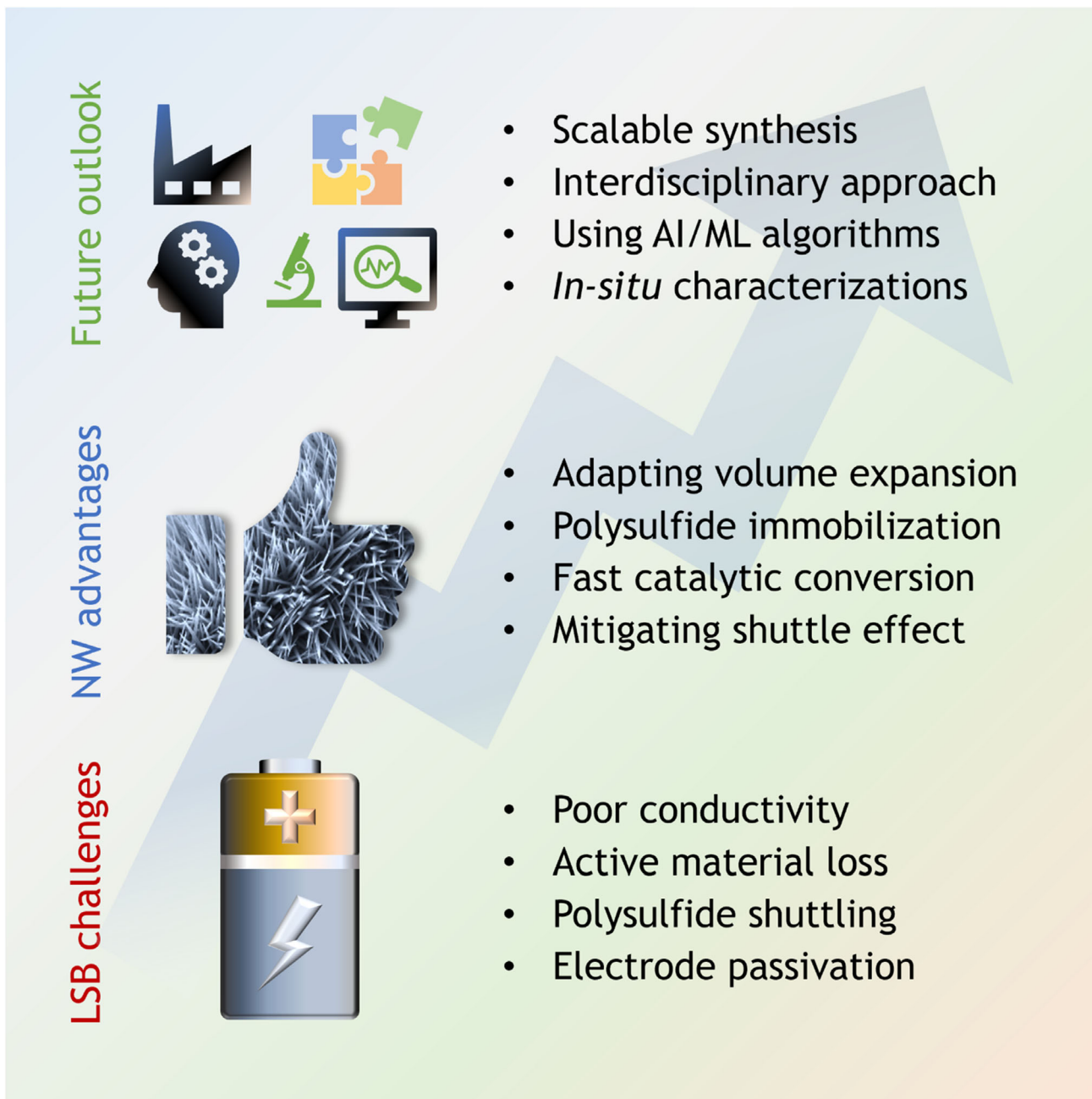


# Next-Generation Li—S Batteries: Impact of Nanowire-Based Electrocatalysts

Tushar Prashant Pandit, Anweshi Dewan,\* Mariela Gisela Ortiz, Juan M. Pérez, and Mihaela Ramona Buga\*



Li–S batteries (LSBs) with their exceptionally high energy density are considered as a more sustainable, green, and cost-effective next-generation energy storage solutions beyond conventional Li-ion batteries (LIBs). Despite their potential, LSBs encounter some key challenges that constrain their commercialization. To tackle these issues and improve the performances of LSBs, researchers have explored various nanomaterials, among which nanowires (NWs) have emerged as one of the potential candidates. Their high aspect ratio ensures efficient electron-ion transport along their length while confining the movement across the radial direction, thereby regulating the reaction kinetics. Additionally, NWs provide exceptional mechanical strength and

interface stability, contributing to enhanced cyclic stability. This review begins with summarizing the basic electrochemistry of LSBs and the associated major technical challenges. Next, it presents a comprehensive and systematic overview of the contemporary research progress in the application of NW electrocatalysts across various LSB components including cathode, separator, and interlayer, correlating their key roles in boosting electrochemical performances. The employment of *in situ* characterization techniques in these systems has also been discussed to get deeper insights. Finally, the review concludes with an outlook on the anticipated prospects of NWs in the future advancement of high-performance LSBs.

## 1. Introduction

The shrinking costs of battery technologies in 2023 predicted a strong surge in the extensive development of electrochemical energy storage devices (EESDs) by 2030 and beyond.<sup>[1]</sup> Advanced EESDs are actively being developed to meet diverse requirements with enhanced performance, better safety, and integrated multifunctionalities.<sup>[2,3]</sup> With a strong emphasis on upscaling battery technologies across industries and society, Li-ion batteries (LIBs) remain the most mature and long-standing technology.<sup>[4–9]</sup> However, the high costs of the raw materials for LIBs relative to secondary expenses such as equipment, energy, and labor further propel the advancement of alternative battery technologies.<sup>[10,11]</sup> Several next-generation battery technologies such as Li–S batteries (LSBs), are at the laboratory development phase and expected to enter the global market with notable advantages over conventional LIBs, including superior energy density, enhanced safety, and improved cost effectiveness.

LSBs are being thoroughly researched because of their high theoretical energy density of 2600 Wh kg<sup>-1</sup> and specific capacity of 1675 mAh g<sup>-1</sup> along with their safety and cost-efficiency.<sup>[12]</sup> Typically, these are consisted of a sulfur-based cathode incorporating conductive additives and an organic binder, a lithium metal anode and a polymer-based separator soaked in

electrolyte. The separator not only maintains the spatial integrity between the cathode and anode but also functions as an insulating barrier to mitigate the risk of short circuits.<sup>[13–15]</sup> However, LSBs experience significant challenges due to the insulating nature of sulfur, structural transformations of cathodes, severe shuttle effect during repetitive cycling, and instability of the lithium anode.<sup>[16]</sup> Such challenges collectively hinder the effective use of LSBs, requiring novel strategies to improve their performances and reliability.

Several strategies have been approached to mitigate these aforementioned challenges, enhance specific capacity, optimize rate capability, and extend the electrochemical lifespan of LSBs, with “nanomaterials” emerging as one of the most promising techniques.<sup>[17]</sup> 1D nanomaterials of carbon, transition metal dichalcogenides (TMDCs), transition metal oxides (TMOs), polymers, metal-organic frameworks (MOFs), and ceramics have been extensively explored and incorporated into LSBs due to their electronic conductivity and ion migration ability. These materials and their composites give rise to innovative nanostructured materials with tailored morphologies such as nanowires (NWs), nanorods, nanotubes, nanofibers, etc., that efficiently improve the performances of LSBs.<sup>[18]</sup>

Among these, NWs have attracted considerable attention in LSBs due to their high structural stability, large specific surface area, excellent conductivity, enhanced polysulfide retention, and critical role in efficient ion movement. All of these advantages foster them to surpass the performance of nanofibers, nanotubes, and nanorods and position them as a promising candidate in LSBs. The porous nature of NWs offers plentiful active sites for electrochemical redox reactions as well as accommodates volume expansion during cycling. They also facilitate efficient electron transfer and ion diffusion by providing optimized conductive pathways.<sup>[19]</sup> In addition, NWs can be easily grown on various nanomaterials and flexible substrates to create free-standing flexible electrodes, which makes them an ideal choice for advanced LSB applications.<sup>[20,21]</sup>

A significant number of review articles on LSBs have primarily focused on the key components such as advancements in sulfur cathodes, separator functionalization, anode

T. P. Pandit, M. G. Ortiz, J. M. Pérez  
Department of Electrical Energy Storage  
Iberian Centre for Research in Energy Storage (CIIAE)  
Avda. de las Letras, s/n, Campus University of Extremadura, 10003  
Caceres, Spain

A. Dewan, M. R. Buga  
ROM-EST Laboratory  
ICSI Energy Department  
National Research and Development Institute for Cryogenic and Isotopic  
Technologies—ICSI  
4 Uzinei, 240050 Ramnicu Valcea, Romania  
E-mail: anweshi.dewan@icsi.ro  
mihaila.buga@icsi.ro

© 2025 The Author(s). *Batteries & Supercaps* published by Wiley-VCH GmbH.  
This is an open access article under the terms of the Creative Commons Attribution License, which permits use, distribution and reproduction in any medium, provided the original work is properly cited.

modifications, and the multiple roles of electrolytes.<sup>[22–26]</sup> However, the critical role of NW-based electrocatalysts in LSBs is not yet comprehensively explored. Considering this as an opportunity to bridge this research gap and unveiling new frontiers in NW electrocatalysts for LSBs, this review provides a thorough analysis of the impact of these materials in mitigating the elemental challenges of LSBs. While this review focuses on the role of NW-based electrocatalysts in cathodes, separators, and interlayers, it is worth mentioning that NWs have also been explored to improve lithium anode stability as well. Interested researchers are referred to related studies for further insights.<sup>[27–32]</sup> Our article first begins by outlining the fundamental working principle of LSBs and the relevant technical challenges, followed by a discussion on the advantages of NWs in LSBs, emphasizing their contributions in charge transport kinetics, polysulfide confinement, and mechanical resilience. Thereafter, a systematic and comprehensive overview of the state-of-the-art research progress on NWs in LSBs is presented, covering different types of NWs in different LSB components such as cathode, interlayer, and separator. Finally, based on the current and past research developments, insights into remaining challenges are given and a forward-looking perspective on the future development of advanced NW-based architectures for next-generation LSB applications is provided.



**Tushar Prashant Pandit** is currently studying for his Ph.D. degree in the department of electrical energy storage, Iberian Centre for Research in Energy Storage (CIAE) and Autonomous University of Madrid (UAM). His research interests focus on advanced high-energy density battery technologies, such as lithium–sulfur batteries and metal–air batteries. He is currently working on the development of novel sulfur hosts materials for lithium–sulfur batteries, as well as interface studies of metal–air batteries using advanced characterization techniques, including operando Raman and infrared spectroscopy.

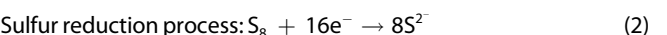
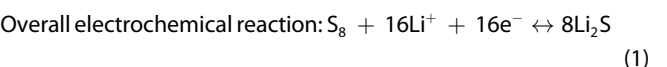


**Anweshi Dewan** earned his Ph.D. in Physics from the Indian Institute of Science Education and Research (IISER), Pune. Then, he worked as a Postdoctoral fellow in the Department of Mechanical Engineering at Korea Advanced Institute of Science and Technology (KAIST). Currently, he is an Assistant Scientific Researcher at the ICSI Energy Department, National Research and Development Institute for Cryogenic and Isotopic Technologies—ICSI, Romania. His research focuses on next-generation energy storage systems, including zero-excess metal batteries (Li and Na), Li–S, and metal–air batteries.

## 2. Fundamental Working Principle and Key Challenges of LSBs

### 2.1. Fundamental Working Principle

In 1962, Herbert and Ulam first introduced sulfur as a positive electrode material in LSBs.<sup>[33]</sup> Figure 1a presents the schematic diagram of a typical LSB, which comprises of a sulfur-based positive electrode, a lithium foil as the negative electrode, and an organic electrolyte as the ion-conducting medium. During the discharge process, sulfur undergoes a multistep electrochemical reduction by lithium ions, leading to the formation of lithium polysulfide (LiPS) intermediates ( $\text{Li}_2\text{S}_8 \rightarrow \text{Li}_2\text{S}_2$ ), with  $\text{Li}_2\text{S}$  as a final discharge product. Upon charging, this reaction is reversed and  $\text{Li}_2\text{S}$  undergoes electrochemical decomposition, regenerating sulfur and lithium.<sup>[34–36]</sup> The electrochemical redox reactions governing the basic operation of LSBs are represented by the following equations.<sup>[37]</sup>



**Mariela Gisela Ortiz** received her Ph.D. in Engineering with a mention in Materials from National Technological University of Argentina. She is currently a Senior Researcher in the department of electrical energy storage, Iberian Centre for Research in Energy Storage (CIAE) in Spain. Her background is in energy storage materials, with a focus on lithium-based technologies aimed at enhancing energy density, potential, and cycling stability using nonpolluting, commercially available, and accessible materials.



**Juan M. Pérez** received his Ph.D. in Chemical Engineering from the Complutense University of Madrid. Currently, He is a director of the electrical energy storage area at Iberian Centre for Research in Energy Storage (CIAE) in Spain. He is a incharge of new projects addressing new materials for batteries and other energy storage systems (supercapacitors, redox flow batteries) together with developments in Circular Economy topics for both current commecial models (alkaline, lithium primary, and ions) and for new incoming (metal–air, flow batteries).



**Mihaela Ramona Buga**, a research scientist at ICSI and leader of the ROM-EST Battery Development Lab since 2019, began her work in the battery field in 2013 as part of the team that proposed and implemented the ROM-EST project, establishing a Laboratory for Energy Storage Technologies at ICSI. Her expertise includes process development, electrode optimization, nanostructured materials, and green battery chemistries, with experience in electrode scale-up, electrochemical testing, surface modification, and sustainable manufacturing.

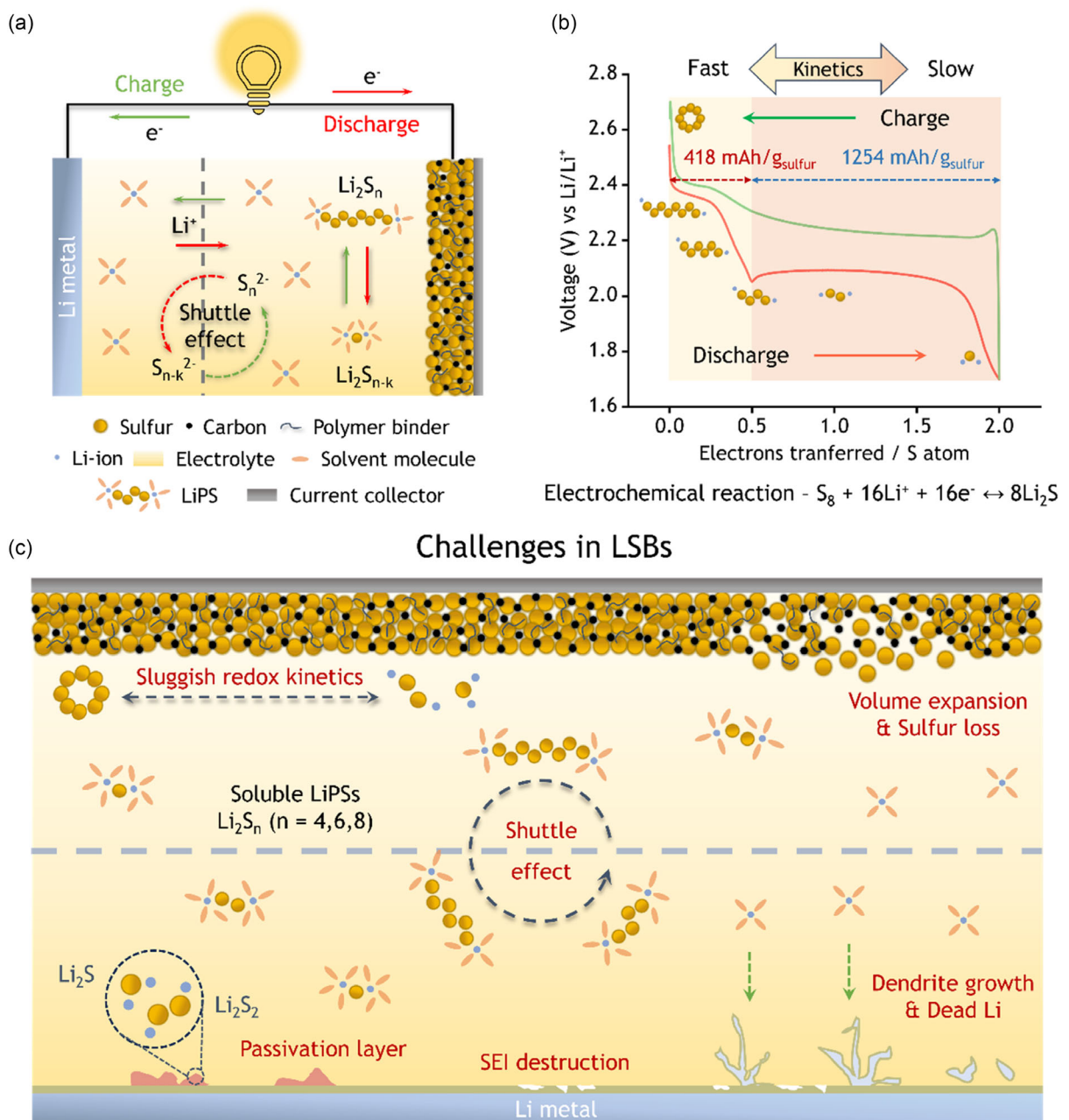


**Figure 1.** a) Schematic diagram illustrating the working principle of a typical LSB, which illustrates the conversion of LiPSs during charging/discharging and shuttling of dissolved LiPSs through the separator. b) A typical charge–discharge curve of a LSB shows the conversion of LiPSs at different stages of charging–discharging and also demonstrates different reaction kinetics, involved with the electron transfer number per S atom. c) Commonly encountered challenges in LSBs such as intrinsic low conductivity of sulfur and lower order LiPSs; sluggish reaction kinetics; volume expansion of cathode material and regular loss of active sulfur; polysulfide shuttling through the separator and growth of passivation layer on the lithium anode; instability of the SEI layer; volume expansion of the metal anode; growth of dendrite; dead lithium and their strong reactivity with the electrolyte leading to the irreversible loss of electrolyte, etc.

The high-capacity lithium anode (3860 mAh g<sup>-1</sup>) and a sulfur cathode with theoretical capacity of 1675 mAh g<sup>-1</sup>, enabled by the 2-electron redox reaction in LSBs predicts a high theoretical energy density of 2600 Wh kg<sup>-1</sup> (gravimetric) or 2200 Wh L<sup>-1</sup> (volumetric) for the LSBs, overcoming the traditional LIBs by nearly an order of magnitude.<sup>[38]</sup>

During a typical discharge process, two prominent voltage plateaus are observed in the discharge curve at 2.3 and 2.1 V

versus Li/Li<sup>+</sup> as presented in Figure 1b. The first plateau at 2.3 V corresponds to a solid–liquid phase transition where solid cyclic sulfur (S<sub>8</sub>) molecule undergoes reduction, leading to its conversion to linear long-chain and intermediate LiPSs (Li<sub>2</sub>S<sub>x</sub>, 4 ≤ x ≤ 8) (fast kinetics region in Figure 1b), equivalent to a theoretical capacity of 418 mAh g<sup>-1</sup> (0.5 e<sup>-</sup> transfer for each S atom). These higher-order PS ions are highly soluble and consequently the reaction kinetics in the first discharge plateau are fast.<sup>[39]</sup> As

the discharge continues, the lower discharge plateau appears at 2.1 V and the electrochemically unstable long chain polysulfides starts to dissociate into solid insoluble  $\text{Li}_2\text{S}_2/\text{Li}_2\text{S}$  species, which corresponds to 1254 mAh g<sup>-1</sup> (1.5 e<sup>-</sup> transfer per S atom). The reaction kinetics involved in this stage including the conversion between solid  $\text{Li}_2\text{S}_2$  and  $\text{Li}_2\text{S}$  are relatively slower than the ones in the upper discharge plateau due to the reduced electrochemical activity and solid-state reactions.<sup>[40]</sup> Due to the high solubility of the higher order PS anions in most of the liquid electrolytes, they can freely migrate between cathode and anode during charging-discharging, which is very commonly known as polysulfide shuttling in LSBs.<sup>[41]</sup> This progressively prevents further electrochemical activity and reduces charge transfer efficiency, leading to passivation of lithium anode, capacity fading, and limiting the practical utilization of sulfur. During the charging process, the electrochemical reaction proceeds in the opposite direction with two potential plateaus at ca. 2.2 and 2.5 V versus  $\text{Li}/\text{Li}^+$ . These plateaus correspond to the stepwise oxidation of insoluble  $\text{Li}_2\text{S}_2/\text{Li}_2\text{S}$  to soluble  $\text{Li}_2\text{S}_x$  ( $4 \leq x \leq 8$ ) and subsequent reformation of the solid sulfur at the cathode. The overall electrochemical reaction is associated with the solid-liquid, solid-solid phase transition, structural and morphological transformations of the cathode, critically impact LSB performance, and cyclic stability.<sup>[42]</sup>

Although it is important to note that determining the exact sulfur reduction mechanism remains the major challenge due to its inherent complexity, it varies depending on many factors such as electrolyte composition, the instability of the LiPSs, and its tendency to react with moisture and oxygen, which leads to undesirable side reactions and can significantly influence the redox processes. Furthermore, the sulfur cathode itself is inherently unstable, leading to self-discharge and capacity degradation over time. These intrinsic complexities pose significant challenges to precisely understand the LSB reaction mechanism.<sup>[40,43]</sup>

## 2.2. Key Challenges

Despite the exceptional theoretical energy density, LSBs have not yet hit the market due to several challenges associated with them (Figure 1c). The first challenge is the insulating nature of sulfur and some intermediate conversion products ( $\text{Li}_2\text{S}_x$ ,  $1 \leq x \leq 2$ ). At room temperature, the electrical conductivity of sulfur and  $\text{Li}_2\text{S}$  is as low as  $5 \times 10^{-30}$  and  $3.6 \times 10^{-7}$  S cm<sup>-1</sup>, respectively. This causes substantial internal resistance, severely limiting the electrochemical reaction kinetics of the active materials. Consequently, the insufficient usage of the active material leads to reduced practical specific capacities, lower energy densities, and overall diminished battery performance.<sup>[44]</sup> The second formidable issue is the large volume expansion of sulfur. The significant difference in the densities of  $\text{Li}_2\text{S}$  (1.66 g cm<sup>-3</sup>) and elemental sulfur (2.07 g cm<sup>-3</sup>) leads to a volume change of approximately 80% within the active materials during repetitive charge/discharge cycles. This induces mechanical stress, leading to electrode cracking, loss of electrical contact, and the formation of inactive regions within the cathode structure. Over prolonged

cycling, this volume expansion contributes to structural degradation and capacity fading and directly affects its long-term cycling stability.<sup>[45]</sup> The third critical issue is the shuttle effect or the polysulfide shuttling. The high solubility of the long-chain polysulfides ( $\text{Li}_2\text{S}_x$ ,  $6 \leq x \leq 8$ ) in liquid organic electrolytes primarily in ether-based ones leads to the uncontrollable migration of LiPSs between cathode and anode during electrochemical cycling. Although, the recurrent dissolution and deposition of polysulfides play a crucial role in facilitating sulfur redox kinetics and enhancing charge transfer within the cathode, this process also increases the impedance of the active material over time by passivating the cathode and inhomogeneous distributing sulfur. LiPSs diffuse through the separator toward the lithium anode, where they undergo reduction reactions to form insoluble insulating  $\text{Li}_2\text{S}$ . This gradually passivates the lithium anode and causes the irreversible loss of active sulfur material, further leading to progressive capacity fading. This also exacerbates cell polarization and limits charge transfer. The shuttling of LiPSs also promotes the overcharge phenomenon, as the higher-order polysulfides partially get reduced by the anode, causing the charging capacity to significantly exceed the discharging capacity, leading to significantly low Coulombic efficiency (CE).<sup>[46,47]</sup> The fourth crucial topic is the sluggish redox kinetics. Due to incomplete sulfur conversion, residual  $\text{Li}_2\text{S}$  remains trapped within the cathode matrix, leading to higher overpotential and uncontrollable polarization. The successive cycling worsens these limitations and results in active material loss, diminished specific capacity, and decreased energy density.<sup>[45,48]</sup> The fifth problem is regarding the instability of lithium metal anode. Nonuniform  $\text{Li}^+$  ion flux induces irregular nucleation, causing dendritic lithium deposition during charging and gradual generation of dead lithium. These lead to an increase in polarization, low CE, and capacity loss. More critically, excessive dendrite growth can pierce the separator, resulting in internal short circuits and thermal runaway, posing severe safety risks. Additionally, highly reactive lithium metal spontaneously reacts with the electrolyte to form the solid-electrolyte interphase (SEI) layer, but the large volume variation damages the SEI layer and irreversibly consumes the lithium as well as the electrolyte. Along with this, the passivation layer formed by the  $\text{Li}_2\text{S}$  layer due to the shuttle effect also hinders the electrochemical activity of the lithium anode as previously discussed.<sup>[13]</sup> The sixth major challenge is self-discharge. This occurs due to gradual dissolution of active cathode materials in electrolyte and continuous LiPS shuttling even when the battery is not in use, leading to a drop in open-circuit voltage (OCV), loss of upper discharge plateau, and capacity degradation. Over time, the self-discharge significantly reduces battery lifespan and may cause premature failure, which is a major challenge for industrial applications.<sup>[45,47]</sup>

The aforementioned challenges are well-recognized and extensive research has been conducted to address them. Numerous strategies have been explored, including rational design and engineering of suitable electrodes and electrolytes, integration of functional interlayers, and modification of separators. However, for the successful commercialization of LSBs, a holistic approach is imperative, ensuring that all component-related challenges are concurrently addressed.

### 3. Importance of NW-Based Electrocatalysts in LSBs

NWs have been extensively investigated in EESDs, especially in several components of the LSB systems to remediate the aforementioned challenges, which will be discussed in the upcoming sections. However, before delving into that, we want to give a crisp overview of the advantages offered by NWs, used in LSB components.<sup>[18,49–51]</sup> These include the following: (a) *high surface to volume ratio*—NW-based electrodes provide high surface area for the electrode–electrolyte contact and enhance the accessibility of the electroactive sites, which increases the material utilization and specific capacity of the battery; (b) *high conductivity*—NWs offer a continuous electron transport pathways through their axial length as well as present short ion-diffusion channels along their diameter, which is critically beneficial for the intrinsically low conductive sulfur and the final discharge products ( $\text{Li}_2\text{S}_2$  and  $\text{Li}_2\text{S}$ ). In addition, it also improves the reaction kinetics and rate capability of the batteries; (c) *structural stability and adapting volume expansion*—the NW structures offer adequate flexibility and structural integrity as well as depending on the porosities, and they can effectively accommodate the volume expansion issues on the sulfur cathodes during charging/discharging. This alleviates the structural deterioration of the electrodes and improve the cyclic stability; (d) *suppressing shuttle effect and promoting polysulfide reaction kinetics*—functional NWs based on polar metal oxides, nitrides, carbides, and sulfides used as LSB cathodes can act as excellent sulfur hosts due to their strong adsorption capability, high surface area, and efficient catalytic activity. Additionally, NWs used as a coating layer on separators of LSBs also help to suppress the polysulfide shuttling effect issue by entrapping the dissolved polysulfides and extend the stability of the sulfur cathodes; and finally, (e) *development of free-standing electrodes*—NWs can be grown *in situ* on different substrates for the development of free-standing electrodes or as a backbone to synthesize different composite electrodes, which subsides the requirement of polymeric binder materials for the electrode preparations. By leveraging these aforesaid features, NWs are widely researched in LSBs to subside the major challenges and promote their practical applications.

### 4. Role of NWs in LSB Components

#### 4.1. Cathode

Till date, numerous strategies have been explored to tackle the predominant challenges in LSB. Various carbon-based materials are explicitly engineered as a sulfur host to (i) accommodate the breathing of sulfur cathodes within their porous architectures during repeated cycling, (ii) provide an electronically conductive framework, and (iii) suppress the severe shuttle effect of LiPSs.<sup>[16]</sup> Typically, there are two ways to immobilize and anchor polysulfides into the sulfur host materials—physical confinement and chemical binding. In the physical confinement, the LiPSs are

confined through porous or layered structure. Carbon-based materials such as porous carbon, graphene, and carbon nanotubes (CNTs) are the promising porous materials for confining the LiPSs owing to their high specific surface area, high porosity, and high electrical conductivity, whereas in the case of chemical binding, polar materials such as TMOs, transition metal sulfides (TMSs), conductive polymers, and MOFs are significantly considered to anchor LiPSs because it has a capability to strongly interact with the polar LiPSs. The fundamental factors such as porosity, high specific surface area, micro/nanostructure, electrical conductivity, and strong polarity of the materials are of utmost importance, as they synergistically contribute to high sulfur loading, greatly confine LiPSs, and enhance the long-term cyclic stability.<sup>[52]</sup>

##### 4.1.1. Metal Oxide-Based NWs

In the work by Chen et al.,<sup>[21]</sup>  $\text{NiCo}_2\text{O}_4$  nanofiber array-deposited carbon cloth ( $\text{CC}@\text{NiCo}_2\text{O}_4$ ) was employed as a sulfur host material for high sulfur loading and successful anchoring of LiPSs (Figure 2a). The intrinsic polar nature of  $\text{NiCo}_2\text{O}_4$  enables high adsorption of LiPSs, thus preventing it from shuttling. The synthesized  $\text{S/CC}@\text{NiCo}_2\text{O}_4$  nanofiber arrays (Figure 2b) served as an electrocatalyst for accelerating the redox conversion kinetics of LiPSs. The cyclic voltammetry (CV) profiles (Figure 2c) reveal that the NWs effectively help in charge transfer process by providing abundant active sites for the stepwise sulfur conversion reactions (from  $\text{S}_8$  to  $\text{Li}_2\text{S}$  and vice versa) across a range of scan rates. The nanofiber arrays grown on the carbon cloth form a 3D interconnected conductive porous network, which establishes an interface between  $\text{NiCo}_2\text{O}_4$  and sulfur active material by facilitating efficient charge transportation. Moreover, nanofiber arrays not only reduce the sulfur agglomeration and accommodate volume variation during cell operation, but also prevent the electrode from cracking or delamination, ensuring long-term cyclic stability. Likewise, Liu et al.<sup>[20]</sup> reported that the Zn-doped  $\text{NiCo}_2\text{O}_4$  NWs grown on carbon cloth (ZNCO-CC) can significantly accommodate the sulfur and its volume variation during battery cycling. The presence of higher valent  $\text{Co}^{3+}/\text{Co}^{2+}$  and  $\text{Ni}^{3+}/\text{Ni}^{2+}$  redox pairs in  $\text{NiCo}_2\text{O}_4$  certainly helps to create multiple polar adsorption sites, which form Ni–S and Co–S bonds with polysulfides, while the final mesoporous Zn-doped structure contributes to more electrolyte infiltration and further enhancement of the electron conductivity across electrode.

In another approach, Selabi et al.<sup>[53]</sup> designed ferromagnetic and defect-rich  $\text{Fe}_3\text{O}_4$  NWs on carbon cloth ( $\text{Fe}_3\text{O}_4\text{-CC}$ ) via a morphology-controlled growth technique. Figure 2d presents the SEM image of conic-shaped  $\text{Fe}_3\text{O}_4$  NWs with  $4.5 \text{ mg cm}^{-2}$  of  $\text{Fe}_3\text{O}_4$  loading (FOC3). The synthesized  $\text{Fe}_3\text{O}_4$  NWs provide multiple electrochemically active nucleation sites for the deposition and subsequent oxidative conversion of  $\text{Li}_2\text{S}$ , which boost up the active material utilization and mitigate LiPS shuttling. FOC3@S cathode exhibits high initial capacity of  $1488.6 \text{ mAh g}^{-1}$  at  $0.1 \text{ C}$  under high sulfur loading ( $5.6 \text{ mg cm}^{-2}$ ), with excellent cycling stability (Figure 2e,f). Selabi et al.<sup>[54]</sup> also fabricated  $\text{Co}_3\text{O}_4$

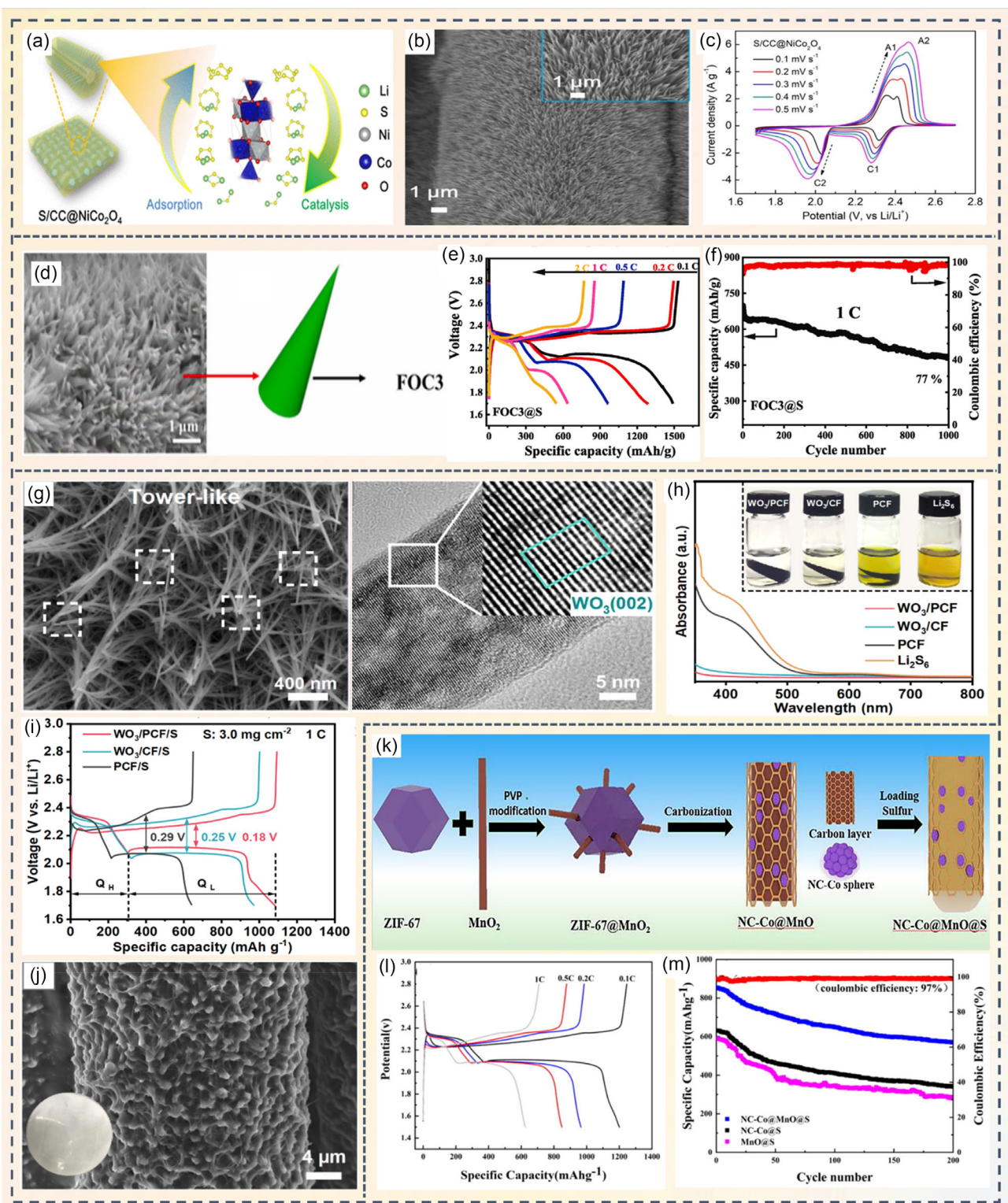


**Figure 2.** a) Schematic presents the working strategy of  $S/CC@NiCo_2O_4$  nanofiber arrays composite; b) SEM image of  $CC@NiCo_2O_4$  composite; c) CV profiles of  $S/CC@NiCo_2O_4$  composite at different scan rates, reproduced with permission.<sup>[21]</sup> Copyright 2021, American Chemical Society. d) SEM image of  $Fe_3O_4$ -CC NWs with  $4.5 \text{ mg cm}^{-2}$   $Fe_3O_4$  (FOC3) content; e) GCD profiles of FOC3@S cathode at different C rates; and f) long-term cyclic stability with CE at 1 C. Reproduced with permission.<sup>[53]</sup> Copyright 2025, Elsevier. g) SEM image of  $WO_3$ /PCF and TEM image of a single  $WO_3$  NW; h) digital photographs and UV-Vis spectra of LiPS solution after the adsorption test; i) 1st cycle GCD data of  $WO_3$ /PCF/S and other electrodes at 1 C current density with  $3 \text{ mg cm}^{-2}$  sulfur loading; j) postcycling SEM image of  $WO_3$ /PCF/S cathode and photo of the separator (inset) after 200 cycles at 1 C. Reproduced with permission.<sup>[56]</sup> Copyright 2025, Royal Society of Chemistry. k) Schematic illustration of synthesis of  $NC-Co@MnO@S$  composite; l) GCD profiles of  $NC-Co@MnO@S$  composite; m) comparison of long-term cyclic stability and CE at 0.5 C. Reproduced with permission.<sup>[57]</sup> Copyright 2021, Elsevier.

NWs grown on carbon cloth ( $\text{CC}@\text{Co}_3\text{O}_4$ ) via crystal-strain modulation for enhancing the adsorption and catalytic conversion of LiPSs. By modulating the crystallite size and resulting degree of lattice strain, catalyst's coordination and electronic band structure were optimized. The resulting  $\text{S}/\text{CC}@\text{Co}_3\text{O}_4$  electrode promotes electron density, superior charge transportation kinetics, and surface utilization, thereby contributing to the excellent electrochemical stability over 1000 cycles at 1 C.

In another study, Diao and coworkers<sup>[55]</sup> synthesized 3D graphene/ $\text{WO}_3$  NW composite as a sulfur host cathode, which provides an excellent conductive porous framework with h- $\text{WO}_3$  NWs, effectively traps the LiPSs, and improves active material utilization. The composite cathode delivered an initial specific capacity of 1410  $\text{mAh g}^{-1}$  at 0.1 C with a capacity decay of 0.086% per cycle. Wang et al.<sup>[56]</sup> developed  $\text{WO}_3$  NW clusters on the core–shell porous carbon fibers ( $\text{WO}_3/\text{PCF}$ ). Due to the structural synergy, the core–shell structure of PCF along with  $\text{WO}_3$  nanoclusters on it acted as an efficient host to accommodate sulfur, buffer the volume fluctuation, and prevent sulfur loss and also functioned as a potent sulfur redox mediator. The  $\text{WO}_3$  NWs present “tower-like” structures with individual NW having average length and diameter of 1  $\mu\text{m}$  and 15–25 nm, respectively (Figure 2g). These bifunctional NWs demonstrate their activity by immobilizing polysulfides through strong polar interaction, alongside accelerating the sulfur catalytic conversion. Consequently, the  $\text{WO}_3/\text{PCF}/\text{S}$  cathode demonstrates high capacity and excellent cycling stability with minimal capacity decay over 1000 cycles at 0.5 C even with high sulfur loading of 6.1  $\text{mg cm}^{-2}$ . The LiPS adsorption test demonstrated that  $\text{Li}_2\text{S}_6$  solution with  $\text{WO}_3/\text{PCF}$  electrode exhibit almost complete decoloration over time, indicating its strong LiPS adsorption ability, which is further corroborated by the UV-Vis data, showing the disappearance of  $\text{Li}_2\text{S}_6$  absorption peak around 411 nm (Figure 2h). The galvanostatic charge–discharge (GCD) profile (Figure 2i) of the  $\text{WO}_3/\text{PCF}/\text{S}$  cathode exhibited an initial specific discharge capacity at 1082  $\text{mAh g}^{-1}$  at 1 C with a sulfur loading of 3.0  $\text{mg cm}^{-2}$  and minimal polarization (0.18 V). Furthermore, the post cycling (after 200 cycles at 1 C) SEM analysis and digital photograph (Figure 2j) reveal that the separator from the disassembled cells with  $\text{WO}_3/\text{PCF}/\text{S}$  cathode displaying a pale-yellow color, thereby confirming the suppression of shuttle effect due to the physical constraint and simultaneous LiPS adsorption by PCF and  $\text{WO}_3$ .

Li and coworkers<sup>[57]</sup> synthesized  $\text{MnO}_2$  NWs via simple hydrothermal method, followed by embedding those into ZIF-67 structures using polyvinyl-pyrrolidone (PVP) as binder. The ZIF-67@ $\text{MnO}_2$  structure was then undergone through carbonization at high temperature to produce the final NC-Co@ $\text{MnO}$  structure which was later impregnated by sulfur via melt-diffusion method to form NC-Co@ $\text{MnO}@S$  composite (Figure 2k). During carbonization process, the PVP-modified ZIF-67@ $\text{MnO}_2$  structure collapses and forms a reduced MnO structure with NC-Co coating strongly adhering onto the surface. The composite structure facilitates rapid charge transfer process and aids in the catalytic conversion process of LiPSs, while the presence of nitrogen and cobalt on the porous carbon

structure improves the electronic conduction. Owing to the presence of superior conductive network and multiple electrochemically active sites, NC-Co@ $\text{MnO}@S$  composite cathode achieved an initial capacity of 1175  $\text{mAh g}^{-1}$  at 0.1 C (Figure 2l) and exhibited cyclic stability over 200 cycles at 0.5 C (Figure 2m). Lee et al.<sup>[58]</sup> synthesized sulfur-infused  $\alpha$ - $\text{MnO}_2$  NWs via a melting and recrystallization method. The material exhibited a significantly lower charge transfer resistance compared to pristine sulfur cathode as confirmed by electrochemical impedance spectroscopy (EIS) measurement. The  $\alpha$ - $\text{MnO}_2$ -coated S cathode demonstrated an initial capacity of 1502  $\text{mAh g}^{-1}$ , primarily due to the high electrical conductivity of  $\alpha$ - $\text{MnO}_2$  NWs. In a related study, Shao and his team<sup>[59]</sup> designed a self-supported cathode based on  $\text{MnO}_2$  NWs incorporated with expanded graphite (EG) nanosheets, aiming to obtain a mechanically flexible structure with high electrical conductivity and high sulfur loading. In the self-standing electrode design,  $\text{MnO}_2$  NWs function as the skeleton of the structure with abundant catalytic sites, while EG joins the polar  $\text{MnO}_2$  NWs to achieve the 3D structure along with promoting the electrical conductivity, rapid charge transfer, and the overall electrochemical process. Wang et al.<sup>[60]</sup> developed  $\text{Na}_4\text{Mn}_9\text{O}_{18}$  NWs (NMO) integrated with reduced graphene oxide (rGO) as a sulfur host material. Unlike conventional melt-diffusion method, in this study, sulfur was *in situ* loaded into the host material by directly dissolving sulfur in the NMO/rGO suspension, enabling the formation of uniform NMO/rGO/S microspheres through a single-step synthesis. The spherical structure of the composite can accommodate sulfur and facilitate the volume variation during cycling, while the cross-linking between NMO nanorods and RGO sheet promotes efficient electron-ion transfer pathways. Guo and his team<sup>[61]</sup> reported a binder-free sulfur cathode with high electrochemically active surface area based on  $\text{Li}_4\text{Ti}_5\text{O}_{12}$  NW array (LTOWA) grown on carbon cloth via hydrothermal and subsequent solid state lithiation process. The advantage of LTOWA structure lies in its ability to form Ti–S bonds with migrating polysulfides rather than O–S bonds in conventional  $\text{TiO}_2$  material, in order to overcome the issues of polysulfide shuttling and poor sulfur utilization. Jin et al.<sup>[62]</sup> developed a composite sulfur host cathode using orthorhombic  $\text{Nb}_2\text{O}_5$  ( $\text{T-Nb}_2\text{O}_5$ ) NWs with graphene, which achieved a specific capacity of 917.1  $\text{mAh g}^{-1}$  at 1 C and long-term cyclic stability over 500 cycles.

Among different TMO-based compounds, Ti-based ones exhibit excellent performance owing to their high surface adsorption energies as well as strong chemisorption properties toward sulfur. For example, Cai et al.<sup>[63]</sup> developed bi-phasic titanium oxide NW cloths (TOCs) with cross-linked structure as a highly porous sulfur host candidate. High surface area (270  $\text{m}^2 \text{ g}^{-1}$ ) and abundant electrochemical active sites acted as a reservoir for the LiPSs and facilitated the sulfur redox kinetics. The resulting S/TOCs cathode delivered a specific capacity of 1163  $\text{mAh g}^{-1}$  at 0.1 C. In other related studies, researchers have integrated  $\text{TiO}_2$  NWs to develop free-standing, binder-free cathodes with 3D architecture to enhance conductivity,

increase sulfur loading, and mitigate both volume variation and LiPS shuttling.<sup>[64–67]</sup>

#### 4.1.2. Metal Sulfide/Selenide/Phosphide/Nitride-Based NWs

Beyond metal oxides, other polar transition metal compounds like sulfides, selenides, phosphides, and nitrides are also effective and well-explored materials in the field of LSBs. In light of this, Chen et al.<sup>[68]</sup> developed a hybrid cathode by integrating Fe single atom decorated hollow mesoporous carbon spheres (SAFe-HMCS) with cobalt sulfide NW arrays ( $\text{Co}_x\text{S}_y$  NWs), grown on free-standing carbon cloth substrate. This multifunctional sulfur host collectively incorporates high conductivity of the carbon cloth, physical confinement effect on sulfur in HMCS, chemisorption ability of  $\text{Co}_x\text{S}_y$  NWs, and excellent catalytic conversion efficiency of SAFe. The cell equipped with the sulfur-loaded composite cathode (S-Co@CC/SAFe-HMCS) demonstrates a very high specific capacity of about 1460 mAh g<sup>-1</sup> at 0.1 C and retains a specific capacity of 578 mAh g<sup>-1</sup> after 600 cycles at 1 C.

In another report,<sup>[69]</sup> Chen and his group designed a triple-phase interface of graphene-like carbon clusters on antimony trisulfide NWs ( $\text{C-Sb}_2\text{S}_3$ ) as a multifunctional polysulfide host. The novel design of the interface synergistically enhances the confinement of polysulfides and improves the kinetics of catalytic reactions by introducing conductive centers via interfacial carbon clusters. Figure 3a presents the SEM image of an individual  $\text{C-Sb}_2\text{S}_3$  NW. GCD measurements performed on LSBs using  $\text{C-Sb}_2\text{S}_3$  NW and pure  $\text{Sb}_2\text{S}_3$  cathodes show the impact of graphene-like carbon clusters on  $\text{Sb}_2\text{S}_3$  interface (Figure 3b). Gourdin et al.<sup>[70]</sup> showed an inventive approach where the performances of LSBs were enhanced by introducing Cu NWs into the sulfur cathode. This strategy simultaneously mitigates the conductivity issues of the sulfur cathodes and challenges related to polysulfide shuttling. Introduction of Cu NWs promotes the electrostatic anchoring of the polysulfide anions onto the Cu NWs, initiating *in situ* formation copper sulfide (CuS) on Cu NWs. This enhances the conductivity of the SEI layer as well as reduces the overpotentials related to plating/stripping of lithium on the anode side.

Zhang's group<sup>[71]</sup> designed a selenium-based electrocatalyst, where metallic cobalt selenide ( $\text{CoSe}_2$ ) NW array was grown onto free-standing carbon cloth.  $\text{CoSe}_2$  offers high electrical conductivity and polar interaction toward the dissolved polysulfides by forming S-Co and Li-Se bonds, boosting the redox reaction kinetics of LiPSs. In a related study, Li et al.<sup>[72]</sup> developed a comprehensive strategy to improve the performance of LSBs, exploiting single-phase V-doped  $\text{CoSe}_2$  ( $\text{Co}_{0.9}\text{V}_{0.1}\text{Se}_2$ ) NWs integrated into a 3D metallic scaffold (3MS). 3MS design hosts  $\text{Co}_{0.9}\text{V}_{0.1}\text{Se}_2$  NWs and sulfur inside its porous structure, while eliminating the need of binder and current collectors. Moreover, the incorporation of Janus microspheres of  $\text{C}@\text{TiO}_2$  into the sulfur-loaded 3MS- $\text{Co}_{0.9}\text{V}_{0.1}\text{Se}_2$  structure contributes to the strong chemisorption of LiPSs at the polar  $\text{TiO}_2$  sites and physisorption of nonpolar sulfur at the carbon part. The synergistic effect of this architecture improves overall electrochemical reactions as well as enables

selective Li-ion transport (Figure 3c). Figure 3d presents the high-magnification SEM image of sulfur-loaded 3MS- $\text{Co}_{0.9}\text{V}_{0.1}\text{Se}_2$  structure. The GCD plots (Figure 3e) show a very low polarization value (160 mV) between the charge/discharge plateaus for the cell using  $\text{Co}_{0.9}\text{V}_{0.1}\text{Se}_2$  and the specific discharge capacity of 1414 mAh g<sup>-1</sup> at 0.1 C. Upon cycling at 1 C,  $\text{Co}_{0.9}\text{V}_{0.1}\text{Se}_2$ -based cell with 1.5 mg cm<sup>-2</sup> sulfur loading is capable of retaining a capacity of 525 mAh g<sup>-1</sup> after 1000 cycles, evidently better than the other two cases (Figure 3f). The researchers also developed a large pouch cell with high sulfur loading of 6.8 mg cm<sup>-2</sup>, which can demonstrate a capacity of 700 mAh and maintain a stable capacity up to 70 cycles with 65.7% capacity retention, promoting the potential of the material for future application.

Transition metal phosphides (TMPs) generally possess very high electronic conductivity, unlike TMOs and TMSs; hence, they often receive attention as efficient electrocatalysts.<sup>[73–76]</sup> Li et al.<sup>[77]</sup> developed a free-standing NCNT@Co-CoP-1@S NW cathode with very high sulfur loading of 10 mg cm<sup>-2</sup> and a low E/S ratio of 7  $\mu\text{L mg}^{-1}$ , which retains an areal capacity of 4.4 mAh cm<sup>-2</sup> after 100 cycles at 2 C rate. The heterojunction interface of Co-CoP provides multiple channels for simultaneous ion/electron migration, effectively suppresses the shuttle effect by chemically immobilizing the soluble polysulfides, and catalyzes their subsequent conversion reactions. In another report, Zhang and his coworkers<sup>[78]</sup> developed a new approach by d-band tuning strategy for constructing a microreactor-like S cathode (MLSC) to achieve an ultra-high sulfur loading of 25 mg cm<sup>-2</sup>. In the structure, embedded ion-selective filtration shell into the shallow surface of porous nickel scaffold (PNS) of the MLSC allows selective Li-ion migration, while coexisting PNS and mesoporous  $\text{Ni}_2\text{Co}_4\text{P}_3$  NWs provide high surface area with a conductive network for rapid charge transfer and subsequent sulfur redox reactions (Figure 3g). Figure 3h presents the SEM image of the pristine PNS- $\text{Ni}_2\text{Co}_4\text{P}_3$  NWs. Figure 3i,j features the SEM image and the elemental mapping images for the sulfur-loaded PNS- $\text{Ni}_2\text{Co}_4\text{P}_3$ . Sulfur was loaded within the porous structure of the  $\text{Ni}_2\text{Co}_4\text{P}_3$  NWs, with a major distribution on the PNS surface and the bases of the NWs, enabling strong attachment between the NWs and LiPSs. EIS measurement revealed that MLSC cell exhibited lower charge transfer resistance owing to its configurational merits. Further, LiPS adsorption test over 8 h confirmed efficient suppression of polysulfide migration with MLSC, signifying the importance of the design.

Similar to the TMPs, transition metal nitrides (TMNs) are also well-known for their high electrical conductivity and chemical stability, in consequence those are also widely employed in LSB cathodes.<sup>[79–81]</sup> Mai and his research group<sup>[82]</sup> constructed a hybrid design of 3D nitrogen-doped graphene and titanium nitride NWs (3DNG/TiN) as a self-standing cathode. In the structure, highly porous graphene sheets provide a well-connected conductive pathway for both ions and electrons, while polar TiN NWs embedded on graphene nanosheets chemically anchor the soluble polysulfides to promote their redox conversion and subside the loss of active materials. The interconnected network with multiple micro-sized voids can attain high sulfur loading as

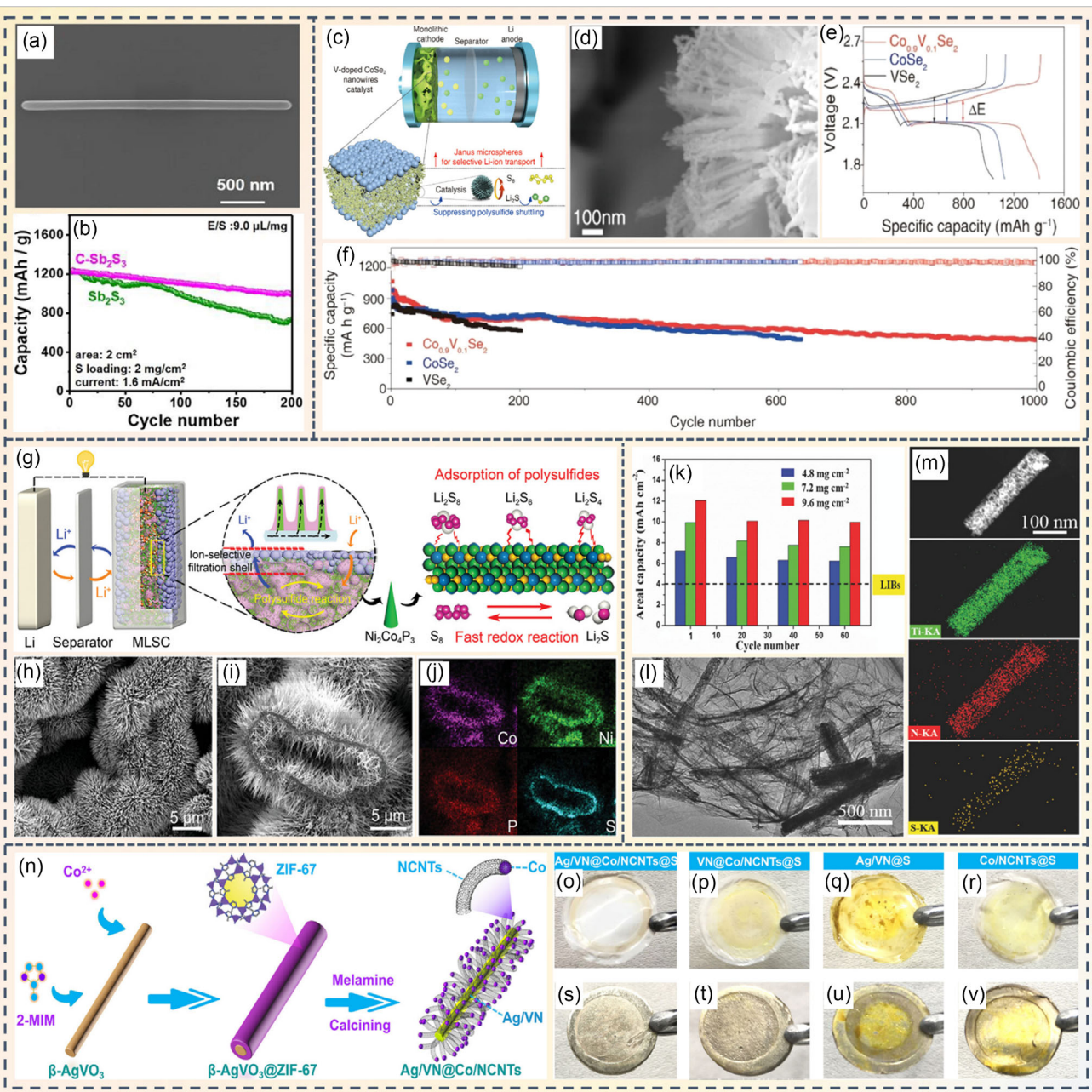


**Figure 3.** a) SEM image of an isolated C@Sb<sub>2</sub>S<sub>3</sub> NW; b) long-term cycling of Li<sub>2</sub>S<sub>6</sub>-based C-Sb<sub>2</sub>S<sub>3</sub> and pure Sb<sub>2</sub>S<sub>3</sub> cells with E/S ratio of 9  $\mu\text{L mg}^{-1}$ . Reproduced with permission.<sup>[69]</sup> Copyright 2021, Elsevier. c) The schematic illustrates the design of 3MS@Co<sub>0.9</sub>V<sub>0.1</sub>Se<sub>2</sub> NWs with the Janus C@TiO<sub>2</sub> microparticles and its multifunctionalities; d) SEM image of S-loaded 3 MS-Co<sub>0.9</sub>V<sub>0.1</sub>Se<sub>2</sub> NWs; e) GCD profiles of the full cells at 0.1 C; f) cyclic stability test of the cells with S-loading of 1.5 mg  $\text{cm}^{-2}$  at 1 C. Reproduced with permission.<sup>[72]</sup> Copyright 2024, American Chemical Society. g) Schematic illustration demonstrates an LSB integrated with MLSC consisting of Ni<sub>2</sub>Co<sub>4</sub>P<sub>3</sub> NWs and ion-selective filtration shell for smooth LiPS trapping, conversion and allowing Li-ion diffusion; SEM images of h) PNS-Ni<sub>2</sub>Co<sub>4</sub>P<sub>3</sub> NWs and i) S-loaded PNS-Ni<sub>2</sub>Co<sub>4</sub>P<sub>3</sub> NWs; j) elemental mapping images of S-loaded PNS-Ni<sub>2</sub>Co<sub>4</sub>P<sub>3</sub> NWs. Reproduced with permission.<sup>[78]</sup> Copyright 2020, Wiley. k) Comparison of areal capacities of cells using 3DNG/TiN cathodes with different sulfur loading; l) post-cycling TEM image of 3DNG/TiN sample (at 0.5 C) and m) TEM elemental mapping images of an isolated NW. Reproduced with permission.<sup>[82]</sup> Copyright 2018, Wiley. n) Schematic illustration of the synthesis of Ag/VN@Co/NCNTs; optical images of o-r) the separators and s-v) lithium anodes recovered from different cells, after cycling. Reproduced with permission.<sup>[86]</sup> Copyright 2021, American Chemical Society.

well as accommodate the volume changes. 3DNG/TiN cathode can sustain a varied range of sulfur loading (4.8–9.6 mg  $\text{cm}^{-2}$ ) upon cycling, as consolidated in Figure 3k. With 9.6 mg  $\text{cm}^{-2}$  of sulfur loading, the cathode can reach an ultrahigh initial areal capacity of 12 mAh  $\text{cm}^{-2}$  and retain 9.96 mAh  $\text{cm}^{-2}$  after 60 cycles at 0.5 C, significantly higher than the commercial LIBs

(4 mAh  $\text{cm}^{-2}$ ). Postcycling (100 cycles at 0.5 C) TEM image of the cycled cathode tells that the cycling doesn't impact the overall cathode morphology (Figure 3l), while corresponding elemental mapping images of a single TiN NW corroborate the strong adsorption of LiPSs on the TiN NW surface (Figure 3m). In a similar article, Zha et al.<sup>[83]</sup> reported a binder-free 3D titanium nitride

(TiN) NW array (NA), directly grown on the carbon cloth as an effective LiPS host. The hierarchical architecture with plentiful inner voids holds high sulfur loading and mitigates volume variations over time.

Among TMNs, vanadium nitride (VN) is also considered as a very promising candidate due to its high electronic conductivity around  $1.67 \times 10^6 \Omega^{-1} m^{-1}$ .<sup>[84]</sup> A study on VN NWs by Li et al.<sup>[85]</sup> reports a novel strategy to design a binder-free, flexible sulfur cathode with core-shell configuration, where S nanodots were embedded into the microporous carbon enclosed mesoporous VN NWs (S/MVN@C NWs). Polar MVN core tethers the active sulfur through physical and chemical interactions, while buffering the stress originated during cycling. The free-standing S/MVN@C NWs cathode provides a conductive pathway for charge migration and achieves an initial capacity of  $1305 \text{ mAh g}^{-1}$  (at 0.2 C) for an areal sulfur loading of  $2.8 \text{ mg cm}^{-2}$ . In a report by Zhan and his team,<sup>[86]</sup> a multifunctional hierarchical host, Ag/VN@Co/NCNTs, was developed using a multistep synthetic procedure, as schematically depicted in Figure 3n. The internal Ag/VN backbone with metallic conductivity ensures rapid charge transfer and provides adsorption sites for redox activity, while the outer part of this structure with porous NCNT arrays accommodates active materials as well as the volume fluctuations during cycling. The Co nanoparticles on top of the NCNTs act as effective adsorption sites for the soluble polysulfides. The Ag/VN@Co/NCNTs@S cathode shows excellent promise in a pouch cell format with an initial capacity of  $1036 \text{ mAh g}^{-1}$  at 0.5 C and conserving  $724 \text{ mAh g}^{-1}$  capacity after 60 cycles. Moreover, the postmortem optical images of the separators (Figure 3o-r) and Li foils (Figure 3s-v) from the disassembled cells confirm that the Ag/VN@Co/NCNTs@S cathode can effectively suppress the polysulfide shuttling and protect the Li anode from corrosion. Overall, the hierarchical architecture of the nanoreactors synergistically promotes the adsorption of LiPSs and electrocatalytic activity through the coordination between internal Ag/VN skeleton and outer Co/NCNTs array.

#### 4.1.3. Other Hierarchical Heterostructure NWs

Pu et al.<sup>[87]</sup> designed CoNiO<sub>2</sub>/Co<sub>4</sub>N NWs decorated graphene composite matrix via *in situ* synthesis process combining hydrothermal and nitridation processes. The CoNiO<sub>2</sub> plays a crucial role in efficient anchoring and promoting LiPS conversion, while Co<sub>4</sub>N improves the electrical conductivity and provides high surface area (Figure 4a). The TEM analysis (Figure 4b) reveals that the heterostructure CoNiO<sub>2</sub>/Co<sub>4</sub>N material possesses uniform NW-like morphology. These NWs form a 3D interconnected conductive matrix in combination with the layered graphene, ensuring the obtained heterostructure provides abundant electrochemical active sites as well as facilitates rapid Li<sup>+</sup> diffusion. The CV profile (Figure 4c) of CoNiO<sub>2</sub>/Co<sub>4</sub>N-G-S displays anodic and cathodic characteristic peaks corresponding to typical polysulfide conversions with low overpotential of 0.263 V, indicating its promising catalytic activity. CoNiO<sub>2</sub>/Co<sub>4</sub>N-G-S cathode delivers a superior capacity of  $1198 \text{ mAh g}^{-1}$  at 0.2 C as illustrated in Figure 4d. The heterostructure cathode achieved an initial capacity of

$688 \text{ mAh g}^{-1}$  and maintained an excellent cyclic stability over 600 cycles at 4 C, with a minor 0.07% capacity decay per cycle (Figure 4e).

In another work, Zhang et al.<sup>[88]</sup> developed cobalt nanoparticle decorated carbon NW arrays coated onto the carbon cloth (CC@Co-CNAs) as a conductive matrix for sulfur materials. This study demonstrates that the formation of Co—S bond effectively enhances the binding between the cathode host and dissolved LiPSs, improving the redox reaction and active material utilization. Davood et al.<sup>[89]</sup> prepared a hierarchical cobalt nanowire/carbon nanofiber/sulfur arrays (CoNWs/CNFs/S) as a sulfur host cathode using a complicated multistep process combining electrodeposition, thermal decomposition of polymer, and infiltration methods. The nanoscale contacts between CoNWs and CNFs improved the electrical conductivity and electrochemical performance, retaining a discharge capacity of  $950 \text{ mAh g}^{-1}$  after 200 cycles.

Luo et al.<sup>[90]</sup> prepared a bifunctional sulfur host cathode featuring *in situ* grown boron carbide NWs on carbon nanofibers (B<sub>4</sub>C@CNF) via a catalyst-assisted strategy (Figure 4f). The sulfophilic B<sub>4</sub>C material provides abundant sites for anchoring polysulfides by strong B—S bonding. B<sub>4</sub>C minimizes the overpotentials of LiPS conversion reactions, whereas the conductive network of B<sub>4</sub>C and CNF collectively accelerates the redox kinetics. The LiPS adsorption study (Figure 4g) revealed that in the presence of B<sub>4</sub>C@CNF material, yellowish Li<sub>2</sub>S<sub>4</sub> solution rapidly became transparent as compared to CNF, suggesting strong affinity of B<sub>4</sub>C toward the LiPSs compared to bare CNF, which adsorbs polysulfides through weak physical interactions. The EIS measurement showed that the pouch cell with B<sub>4</sub>C@CNF electrode with a high sulfur loading (40 mg over a 12 cm<sup>2</sup> area) manifests lower charge transfer resistance in freshly assembled cells than CNF-based cell, although the resistance increases over cycling (Figure 4h).

#### 4.1.4. Polymer-Based Heterostructure NWs

Conducting polymers have also been widely employed as sulfur host cathodes in LSBs; in particular, the functional polymers such as polypyrrole (PPy), polyaniline (PANI), and PEDOT can act as a redox mediator to boost the LiPS conversion and mitigate the severe shuttle effect in LSBs.<sup>[91]</sup> Owing to the excellent electronic conductivity and chemical stability of PANI, Zhang et al.<sup>[92]</sup> employed PANI NWs as a barrier layer on sulfur cathode to restrain the loss of active materials. PANI NWs were directly electrodeposited onto the formerly prepared carbon paper-sulfur cathode. The designed cathode delivered a superior discharge capacity of  $1304 \text{ mAh g}^{-1}$  at  $320 \text{ mA g}^{-1}$  current density, maintaining cyclic stability over 100 cycles with 66.3% capacity retention. Also, Liu et al.<sup>[93]</sup> designed a helix-shaped composite structure, with sulfur particles anchored onto the SiO<sub>2</sub>@C@PANI NWs. Resulting spring-like architecture was able to effectively mitigate the volumetric fluctuations of the sulfur cathode during repeated cycling, while PANI offered high electrical conductivity and strong polysulfide adsorption capability, simultaneously elevating the reaction kinetics and inhibiting

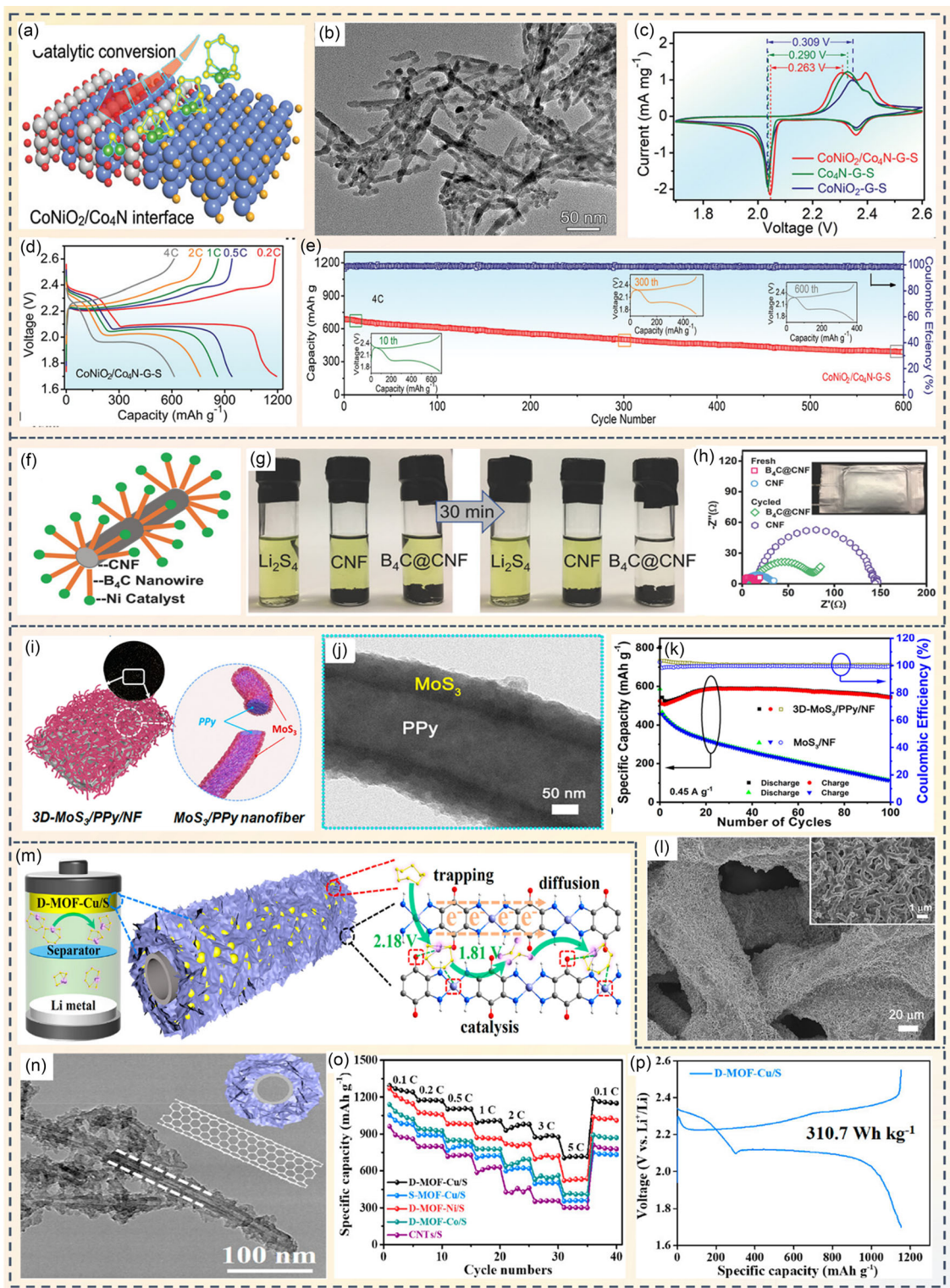


**Figure 4.** a) Schematic illustration of the interaction mechanism between  $\text{CoNiO}_2/\text{Co}_4\text{N}$  heterostructure NWs and polysulfides at their interface; b) the TEM image of the  $\text{CoNiO}_2/\text{Co}_4\text{N}$  heterostructure NWs; c) comparison of CVs of different synthesized materials at  $0.1 \text{ mV s}^{-1}$  scan rate; d) GCD profiles of  $\text{CoNiO}_2/\text{Co}_4\text{N-G-S}$  cathode; e) cyclic stability test at 4 C. Reproduced with permission.<sup>[87]</sup> Copyright 2024, Wiley. f) Schematic illustration of the architecture of the bifunctional  $\text{B}_4\text{C}@\text{CNF}$  cathode; g) digital images of LiPSs adsorption tests; h) EIS data of a pouch cell integrated with a  $\text{B}_4\text{C}@\text{CNF}$  cathode, before and after cycling. Reproduced with permission.<sup>[90]</sup> Copyright 2018, Wiley. i) Schematic illustration of the structure of sulfur equivalent 3D  $\text{MoS}_3/\text{PPy}/\text{NF}$  cathode; j) TEM image of a single heterostructure NW; k) long-term cyclic stability and CE data at  $0.45 \text{ A g}^{-1}$ ; l) SEM image of  $\text{3D}-\text{MoS}_3/\text{PPy}/\text{NF}$  cathode after 100 cycles. Reproduced with permission.<sup>[96]</sup> Copyright 2024, Wiley. m) Schematic illustration of polysulfide trapping and conversion on D-MOF-Cu/S cathode; n) TEM image of D-MOF-Cu-based hierarchical NW; o) C-rate performances of different cathodes; p) GCD of the pouch cell with multilayer D-MOF-Cu/S cathode. Reproduced with permission.<sup>[97]</sup> Copyright 2023, American Chemical Society.

polysulfide shuttling. Wu and his team<sup>[94]</sup> developed birnessite-MnO<sub>2</sub> nanosheets inside the PANI nanotubes (NSs-MnO<sub>2</sub>@PANI) as a sulfur host. Combined DFT and experimental studies confirmed that the induced electric field originated at the interface of PANI/MnO<sub>2</sub> heterostructure due to interfacial rearrangement of charges, produced a strong ion migration channel which eventually enhanced the conductivity for boosting the redox kinetics of sulfur. The NSs-MnO<sub>2</sub>@PANI/S composite cathode achieved a discharge capacity of 1473.7 mAh g<sup>-1</sup> at 0.1 C.

Liu et al.<sup>[95]</sup> constructed a sulfur cathode with conductive mesoporous multiwalled CNT (MWCNT) core and microporous poly-maleimide (PPI) shell (PPI@MWCNT-Y) via an *in situ* single-step polymerization technique. Hierarchical porous conductive architecture with abundant adsorption sites prevents the loss of active materials from cathode, while improving the redox reaction kinetics by facilitating electron and lithium ions transportation. The optimized cathode, S/PPI@MWCNT-47, demonstrated an exceptional initial capacity of 1592.1 mAh g<sup>-1</sup> at 0.2 C. Yu et al.<sup>[96]</sup> constructed a free-standing, binder-free sulfur equivalent cathode, MoS<sub>3</sub>/PPy/NF, by growing MoS<sub>3</sub>/PPy NWs on porous nickel foam (NF) via a combination of electro-polymerization and electrodeposition technique (Figure 4i). TEM image shows that the PPy NWs are coated with MoS<sub>3</sub> nanoparticle layer (Figure 4j). 3D-MoS<sub>3</sub>/PPy/NF cathode exhibited a reversible capacity of 720 mAh g<sup>-1</sup> at 0.09 A g<sup>-1</sup> current density and retained 93% capacity after 100 cycles at 0.45 A g<sup>-1</sup> (Figure 4k). Postmortem SEM analysis (Figure 4l) after cycling shows that 3D-MoS<sub>3</sub>/PPy/NF NWs preserved its overall architecture except thickening of the PPy NWs (inset of Figure 4l). This was indicative to the positive impact of the PPy NWs in mitigating the volume expansion issue of the MoS<sub>3</sub> electrode. This study demonstrated a new strategy of introducing a sulfur equivalent material MoS<sub>3</sub> as cathode in LSBs, eliminating the formation of LiPS intermediates.

#### 4.1.5. Metal-Organic Framework-Based NW Structure

Xiao et al.<sup>[97]</sup> designed hierarchical sulfur hosts via *in situ* axial assembly of dual-active center MOF (D-MOF) NWs on CNTs. As depicted in Figure 4m, D-MOF-Cu features its multifunctionality in terms of efficient immobilization of liquid polysulfides, high catalytic efficiency, and associated fast diffusion of electrons for redox conversion of sulfur. The dual-active centers of D-MOFs offer coordinated metal catalytic centers such as M-N<sub>4</sub> (M: Co, Ni, Cu), which optimize electronic structure and promote metal-sulfur hybridization. The TEM image (Figure 4n) revealed that D-MOFs-Cu flakes are uniformly coated on the CNT skeletons, forming an electrically conductive π-d conjugated hierarchical architecture. Strong polar O sites in D-MOFs help to chemically adsorb the Li<sup>+</sup> ions from the LiPSs, and in particular D-MOF-Cu features its highest ability to stabilize the intermediate LiPS species. D-MOF-Cu/S cathode demonstrated the best rate capability performance among all other sulfur-loaded D-MOF-based cathodes (Figure 4o). In the case of pouch cell, the D-MOF-Cu/S cathode exhibits an impressive energy density of 310.7 Wh kg<sup>-1</sup> (Figure 4p). These results highlight that by tailoring

configurational compatibility and electronic structure in synthesized D-MOFs, the electrochemical performance of LSBs can be significantly improved through the modulation of interactions among different catalytic centers and the polysulfide ions at the molecular/atomic level. A summary of reported NW-based cathode materials and corresponding LSB performances is presented in (Table 1).

## 4.2. Modified Separator and Hybrid Interlayer

In parallel to the ongoing researches on cathode material design, the development of the modified separators and introduction of hybrid functional interlayers between cathodes and separators are also efficient and economical approaches to mitigate the shuttle effect, to reduce the polarization, and for the effective utilization of sulfur in LSBs.<sup>[98–101]</sup> An ideal separator or an interlayer should feature—(i) strong binding capacity to immobilize LiPS for effective suppression of polysulfide shuttling, (ii) excellent catalytic activity to promote the kinetics of LiPS conversion, (iii) superior electronic and ionic conductivity to achieve a good rate capability, and (iv) optimized thickness with high porosity to allow facile migration of solvated lithium ions without affecting the energy density of the battery.<sup>[102,103]</sup> In general, achieving the aforementioned multifunctionalities from a single-component material is not so straightforward; therefore, it is preferred to develop multicomponent hybrid materials for a modified separator or functional interlayer.

### 4.2.1. Modified Separator

The application of multifunctional carbonaceous materials has been an effective approach for modifying the properties of polymer-based separators in LSBs, allowing the trapping of soluble polysulfides to improve the cyclic stability while maintaining the ionic conductivity. In 2016, Zhou et al.<sup>[104]</sup> reported a simple slurry-coating approach to modify the conventional Celgard separator with N-rich porous carbon NWs (N-PCNWs) to address the problem of shuttle effect and inferior electrochemical stability. The cells integrated with N-PCNW separators use pure sulfur as cathode and present a high specific discharge capacity of 1430 mAh g<sup>-1</sup> at 0.2 C. After continuous charging/discharging at 0.5 C for 500 cycles, the cells retain a capacity of 507.6 mAh g<sup>-1</sup> with a capacity decay of 0.08% per cycle. High specific surface area of the NW architecture with N doping improves the battery performances by chemically adsorbing the soluble polysulfides while its high ionic conductivity and fast electron transport efficiently reduce the voltage polarization during charging/discharging cycles.

However, the immobilization of LiPSs by carbon-based materials mostly rely on physical adsorption, leading to poor cyclic stability because of the weaker interaction between the nonpolar carbon materials and the polar LiPSs. The presence of polar groups on the NW structures can significantly improve the conditions. NWs based on polar materials can adsorb the LiPSs firmly through chemisorption process. But the inherent low

Cathode materials	Synthesis methods <sup>a)</sup>	Sulfur infiltration process <sup>a)</sup>	Sulfur contents and electrochemical metrics				Reference
			Sulfur loading [mg cm <sup>-2</sup> ]	E/S ratio [ $\mu\text{L mg}^{-1}$ ]	Cycling performance (C rate)	Retained capacity [mAh g <sup>-1</sup> ]	
<i>Metal oxide-based NWs</i>							
S/CC@NiCo <sub>2</sub> O <sub>4</sub>	HT & TA	MD & C	3.5–8.9	–	200 (0.2)	660	[21]
ZNCO-CC/Li <sub>2</sub> S <sub>8</sub>	HT & TA	APS (Li <sub>2</sub> S <sub>8</sub> )	1.28–5.12	–	200 (0.5)	362	[20]
Fe <sub>3</sub> O <sub>4</sub> -CC@S	HT & TA	MD	1.5–5.6	2.7–6.4	1000 (1)	484.8	[53]
S/CC@Co <sub>3</sub> O <sub>4</sub>	HT & TA	MD	1.5–6.6	4.7–13	1000 (1)	449.9	[54]
3D rGO@WO <sub>3</sub> @S	HT	MD	2–4.6	12	500 (3)	412	[55]
WO <sub>3</sub> /PCF/S	ED, TA, HT, & TA	MD	2.2–6.1	12	1000 (1)	660	[56]
NC-Co@MnO@S	HT, CM, & TA	MD	1.1	20	200 (0.2)	700	[57]
MnO <sub>2</sub> NW/EG	HT, EE, & US	APS (Li <sub>2</sub> S <sub>6</sub> )	1–7	10	500 (1)	538	[59]
NMO/rGO/S	HT & US	M & SD	0.8	–	500 (1)	520	[60]
LTOWA/S	HT & SSR	MD	1.6–4	–	300 (1)	414	[61]
T-Nb <sub>2</sub> O <sub>5</sub> /G/S	HT & TA	MD	1.3–1.7	10	500 (1)	576.7	[62]
S/TOCs	HT & TA	MD	1	20	200 (1)	427.6	[63]
CC/TiO <sub>2</sub> /S	HT & TA	S & TA	1.7–2	–	300 (1)	548	[64]
C-TiO <sub>2</sub> NAs	HT & TA	APS (Li <sub>2</sub> S <sub>8</sub> )	2–4	–	500 (1)	930	[65]
N-TiO <sub>2</sub> NW@CC	HT & TA	APS (Li <sub>2</sub> S <sub>8</sub> )	4.8	–	200 (0.2)	750.2	[66]
TiO <sub>2</sub> NW/G	HT & US	APS (Li <sub>2</sub> S <sub>6</sub> )	3.2	–	200 (0.2)	1053	[67]
<i>Metal sulfide/selenide/phosphide/nitride-based NWs</i>							
S-Co@CC/SAFE-HMCS	HT, SU, TM, C, TA, D, & TA	MD	1	26.5	600 (1)	580	[68]
C-Sb <sub>2</sub> S <sub>3</sub>	ST	APS (Li <sub>2</sub> S <sub>6</sub> )	1–5	7–10	200 (0.2)	600	[69]
C@CoSe <sub>2</sub> /S	HT & SE	S & TA	3–5.1	–	1000 (5)	513	[71]
S-loaded 3 MS-Co <sub>0.9</sub> V <sub>0.1</sub> Se <sub>2</sub>	HT & SE	S & TA	1.5–18.7	2.5	1000 (1)	525	[72]
NCNT@Co-CoP@S	HT, TA & PH	S & TA	4–10	7	900 (5)	603.9	[77]
MLSC	HT & PH	S & TA	5–25	–	1000 (1)	658	[78]
3DNG/TiN	SA & NT	APS (Li <sub>2</sub> S <sub>6</sub> )	4.8–9.6	10	200 (1)	957	[82]
TiN NA	HT & NT	APS (Li <sub>2</sub> S <sub>6</sub> )	1–3	–	500 (2)	690	[83]
S/MVN@C	HT, C & NT	S & TA	1.1–9.7	–	200 (1)	636	[85]
Ag/VN@Co/NCNT@S	HT, SP, & NT	MD	2.8–10.3	10–20	2000 (2)	591.1	[86]
<i>Other hierarchical heterostructure NWs</i>							
CoNiO <sub>2</sub> /Co <sub>4</sub> N-G-S	HT, TA, NT, & M	S & TA	1–3.7	10–15	600 (4)	389	[87]
CC@Co-CNAs	HT, ST, & TA	APS (Li <sub>2</sub> S <sub>6</sub> )	2.5–10	10–13	300 (1)	663	[88]
CoNWs/CNFs/S	TM, TA, & ED	MD	1–1.5	–	200 (1)	950	[89]
B <sub>4</sub> C@CNF	CAS (CM, US, TA)	APS (Li <sub>2</sub> S <sub>6</sub> )	2–10.3	10	500 (1)	815	[90]
<i>Polymer-based heterostructure NWs</i>							
PANI NWs	ED	M & C	3	–	100 (0.2)	725	[92]
SiO <sub>2</sub> @C@PANI/S	SG, C, TA, & PM	MD	–	–	120 (0.1)	940	[93]
NSs-MnO <sub>2</sub> @PANI/S	HT, PE & AT	MD	2–15.9	–	500 (0.2)	699	[94]
S/PPI@MWCNT	PM & C	MD	–	15	400 (1)	677.5	[95]
NCNW@S	PM & TA	MD	1.5	–	200 (0.5)	690	[134]
<i>MOF-based NW</i>							
D-MOF-Cu/S	ST	MD	1.6–14.3	4.3–8.3	1000 (1)	695.9	[97]

<sup>a)</sup>Note: Abbreviations for synthesis methods and sulfur infiltration processes—hydrothermal (HT), solvothermal (ST), thermal annealing (TA), melt-diffusion (MD), coating (C), adding polysulfide solution (APS), electrodeposition (ED), chemical mixing (CM), electrochemical expansion (EE), mixing (M), spray drying (SD), solid state reaction (SSR), ultrasonication (US), template method (TM), sulfurization (SU), doping (D), selenization (SE), phosphidation (PH), soaking (S), self-assembly (SA), solution process (SP), nitridation (NT), catalyst-assisted synthesis (CAS), sol-gel method (SG), polymerization (PM), partial etching (PE), alkaline treatment (AT).

conductivity of these materials often causes the underutilization of the adsorbed LiPSs and inferior rate performance. Therefore, it is attempted to simultaneously incorporate both type of materials in order to substantiate suitable ionic migration and to enhance the redox kinetics of the trapped polysulfides.

Wang et al.<sup>[102]</sup> synthesized a hybrid multifunctional system consisting of polar MnO<sub>2</sub> NWs and nonpolar CNTs, to immobilize LiPS through simultaneous chemical and physical interactions. High conductivity of CNTs also promotes electrochemical reactions and lithium-ion migration. Figure 5a schematically illustrates the structures and functions of pristine (Celgard 2500) and modified polypropylene (PP) separators. LSB module with MnO<sub>2</sub>/CNT-modified PP separator (MC-PP) presents a very high specific capacity of 1315.4 mAh g<sup>-1</sup> at 0.1 C, significantly surpassing others (Figure 5b, GCD profiles at 0.5 C). The LSB cell integrated with separators with an equal weight ratio of MnO<sub>2</sub> and CNTs (50%:50%) exhibited best long-term cyclic performance, with a capacity retention of 68.03% after 500 cycles at 1 C (Figure 5c). In a similar work,<sup>[105]</sup> Cai and coworkers reported the synthesis of porous N-doped CNT-decorated Co-MnO (Co-MnO/NCNTs) heterostructure material with caterpillar-like morphology. The material consisted of a Co-MnO backbone with interconnected N-doped CNTs grown on its surface. It synergistically provides the active sites for physical and chemical adsorption of soluble polysulfides, fast redox conversions of the intermediate polysulfides, and adequate utilization of the active materials, barring their loss during repeated cycling (Figure 5e). LiPS adsorption capabilities of the samples were visually demonstrated by the polysulfide adsorption test, with Co-MnO/NCNTs producing a nearly colorless solution (inset, Figure 5f). Corresponding UV-Vis absorbance spectra (Figure 5f) show the presence of lowest intense LiPS absorption peak for Co-MnO/NCNT sample around 300–450 cm<sup>-1</sup>. Figure 5g showcases the process of LiPS diffusion in H-type cells through the Celgard 2500 separator and the modified one with Co-MnO/NCNTs coating at different time intervals, endorsing superior performance of the former in efficiently inhibiting the shuttle effect.

A modified functional separator incorporating sodium-containing TiO<sub>2</sub>-based hybrid nanowire/nanosheet (STO-W/S) architecture was developed by Ma and his group<sup>[106]</sup> by engineering the surface of a commercial PP (Celgard 2325) separator. Polar structure of STO-W/S presents strong affinity toward LiPSs and increases electrolyte wettability, consequently easing the Li<sup>+</sup> diffusion. This outperforms the overall electrochemical performances of LSBs coupled with pristine PP and STO-W modified PP separators.

Researchers have also explored other metal oxides such as V<sub>2</sub>O<sub>5</sub> for customizing the separators and discovered that amorphous V<sub>2</sub>O<sub>5</sub> (V<sub>2</sub>O<sub>5</sub>, nH<sub>2</sub>O) or VOH perform even better than the crystalline V<sub>2</sub>O<sub>5</sub> in restricting LiPS shuttling. Their intrinsic structural defects induced by the long-range disorders yield ample active sites for polysulfide adsorption and their subsequent redox conversion. Chen et al.<sup>[103]</sup> modified the amorphous VOH NWs by conductive polyaniline (PANI) encapsulation (VOH@PANI) via an *in situ* chemical oxidative polymerization technique. This mechanically stable organic-inorganic heterostructure was

further employed to modify the conventional PP separator, VOH@PANI-PP. The disordered structure of VOH extensively helps the Li-ion migration, while the PANI encapsulation assists in efficient LiPS trapping through the imine (—N=) groups present on its structure as well as uplifts the electronic conductivity to improve LiPS conversion kinetics (Figure 5h). The rate capability plot and EIS measurement show that a cell equipped with VOH@PANI-PP separator surpasses the unmodified one in overall cell performance (Figure 5i,j).

As mentioned previously, TMNs have higher electronic conductivity compared to other TMO materials, which permit them to improve the overall electrochemical performances of the LSBs.<sup>[80,81]</sup> Park et al.<sup>[107]</sup> presents the design of a multifunctional separator based on N-doped carbon-embedded, cobalt-doped titanium nitride (NC-Ti<sub>0.95</sub>Co<sub>0.05</sub>N) NWs. Doping of ferromagnetic particles such as Co induces intrinsic magnetic fields and influences the spin-polarized electrons inside the material. This eventually strengthens the LiPS adsorption and weakens the S—S bonds in low conducting Li<sub>2</sub>S<sub>2</sub> and Li<sub>2</sub>S, accelerating their redox conversions (Figure 5k). The samples demonstrated robust 1D morphology (Figure 5l), which were constituted of evenly distributed nanosized particles with uniform spread of the constituent elements, confirmed by TEM imaging and electron energy loss spectroscopy (EELS) mapping (Figure 5m). GCD measurements (at 0.1 C) offer highest Q<sub>lower</sub>/Q<sub>upper</sub> value of 2.2 (theoretically predicted value is 3) for NC-Ti<sub>0.95</sub>Co<sub>0.05</sub>N NWs@PP separator integrated cells, denoting efficient conversion of Li<sub>2</sub>S<sub>4</sub> to Li<sub>2</sub>S (Figure 5n). The utilization of the ferromagnetic particle-doped electrocatalyst on separator significantly reduces the overpotential of the deposition and oxidation of Li<sub>2</sub>S, also prominent from the CV data (Figure 5o), in terms of reduced polarization voltage and high conversion efficiency of Li<sub>2</sub>S.

Among several metal nitrides, indium nitride (InN) has also demonstrated its competency as an efficient electrocatalyst in LSBs, through its polar nature, high electrical conductivity, and low bandgap. Zhang et al.<sup>[108]</sup> successfully employed the bifunctional InN NW modified separator to successfully entrap the polysulfide anions and improve the electrocatalytic reaction kinetics. The LSB cells with InN NW-modified separator showed a promising discharge capacity of 1430.3 mAh g<sup>-1</sup> at 0.1 C and a better long-term stability with capacity retention of 73.4% after 1000 cycles at 1 C, significantly overcoming the performance of the cells with pristine separator. Indium centers and N-containing electron-rich parts of the conductive molecule chemically anchor the polysulfide anions and lithium ions, simultaneously preventing the loss of active materials and polysulfide shuttling, while improving the redox kinetics.

#### 4.2.2. Hybrid Interlayer

Porous interlayers are in general sandwiched between cathode and separator in LSBs as an assisting layer for easy passage of the lithium ions, adsorption and immobilization of LiPSs as well as their subsequent catalytic conversions.<sup>[109]</sup> Various types of hybrid functionalized catalysts have been used as interlayers

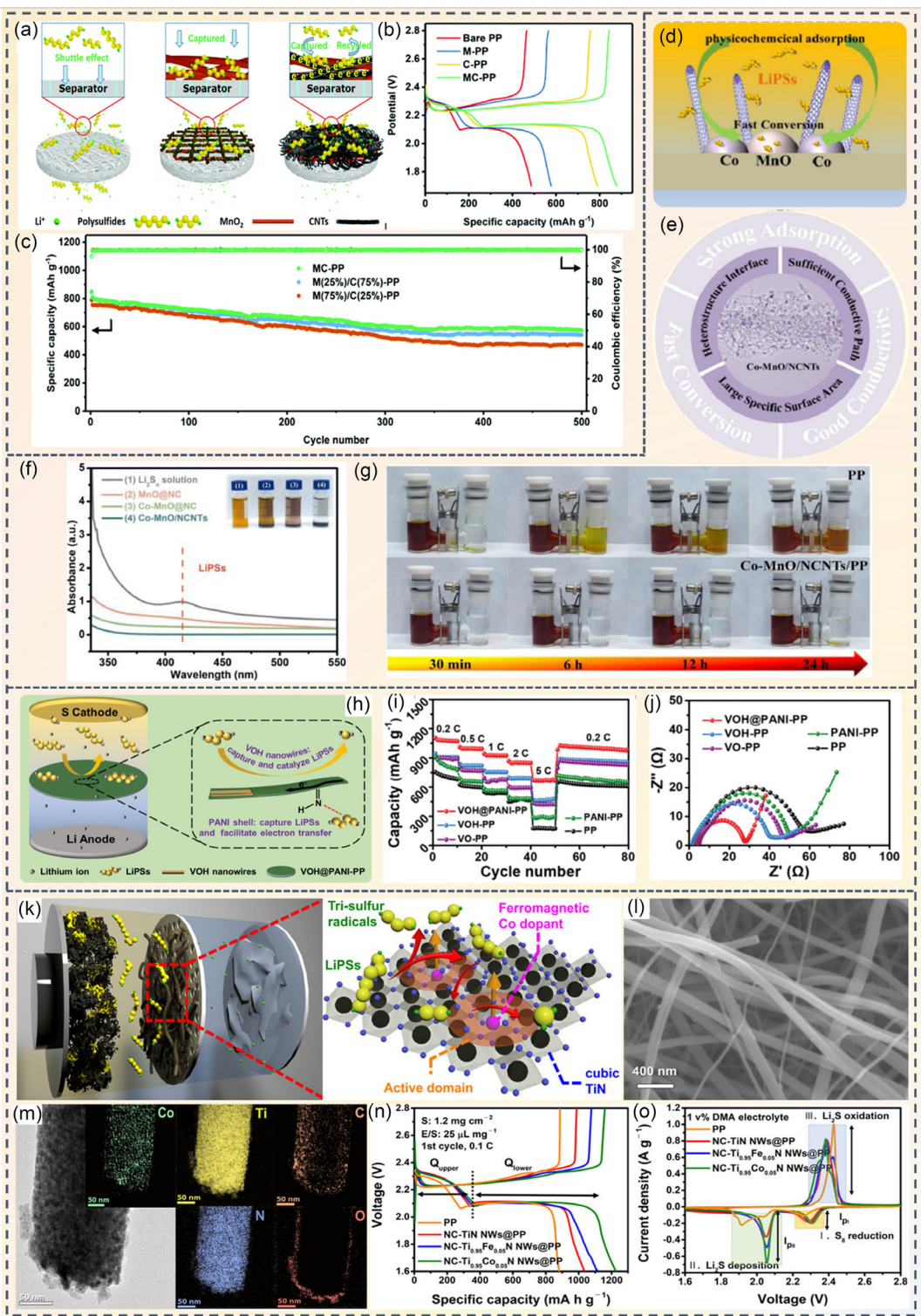


**Figure 5.** a) Schematic presents the electrocatalytic behaviors of pristine PP and modified  $\text{MnO}_2/\text{PP}$ ,  $\text{MnO}_2/\text{CNT}/\text{PP}$  separators in LSB structures; b) typical GCD data of LSBs with different separators at 0.5 C; c) cyclic stabilities of the LSBs using different separators at 1 C. Reproduced with permission.<sup>[102]</sup> Copyright 2019, Royal Society of Chemistry. d,e) Graphical representation illustrates the conductive N-doped CNT decorated Co-MnO material, utilized in separator modification, and involves strong LiPS adsorption by physicochemical route and fast catalytic reactions for LSBs. f) UV-Vis absorbance spectra of the solutions after LiPS adsorption and the corresponding photos in inset; g) comparison of LiPS diffusion over time in H-cells using different separators. Reproduced with permission.<sup>[105]</sup> Copyright 2023, Elsevier. h) Graphical illustration of an LSB module integrated with VOH@PANI-PP separator. Comparison of i) the rate performances; and j) EIS data before cycling of different LSB cells utilizing different separators. Reproduced with permission.<sup>[103]</sup> Copyright 2021, Wiley. k) Schematic demonstrates an LSB cell equipped with NC-Ti<sub>0.95</sub>Co<sub>0.05</sub>N NW-based separator and associated electrocatalytic reaction pathways; l) SEM image and m) TEM image along with the elemental EELS mapping data of NC-Ti<sub>0.95</sub>Co<sub>0.05</sub>N NWs; the comparison of n) GCD and o) CV profiles of different electrocatalysts. Reproduced with permission.<sup>[107]</sup> Copyright 2024, Wiley.

to improve the electrochemical performances altogether. Yu et al.<sup>[110]</sup> synthesized 1D N-doped porous carbon@CNT NWs (CNT@NC) as a bifunctional interlayer for both trapping and catalyzing the polysulfide anions. The synthesis process of the material involves the surface coating of multiwalled CNTs (MWCNTs) with a polymer, followed by its calcination under ammonia environment, which converts the polymer into N-doped carbon (Figure 6a). The MWCNT skeleton provides a continuous pathway for the electron conduction and the porous carbon coating facilitates the physisorption of LiPSs. The doped N atoms induce polarity in the NW structure which boosts the chemisorption of polysulfide ions and helps to suppress the shuttle effect efficiently, followed by their rapid catalytic conversion. The LSB equipped with bifunctional CNT@NC-10 interlayer demonstrates a reversible specific capacity of 550 mAh g<sup>-1</sup> ( $\approx$ 81% capacity retention) after 500 cycles at 2 C, with a cathode sulfur loading of 1 mg cm<sup>-2</sup> (Figure 6b). A novel chemi-functional interlayer structure, consisting of zinc oxide (ZnO) NWs and interconnected conductive network, was developed by Kumar's group,<sup>[111]</sup> having an inspiration from the design of brush-like cell membranes for nutrient adsorption. ZnO NWs were grown on a carbon nanofiber (CNF) mat for ZnO NW growth and it was later placed between the PE separator and S/MWCNT cathode, facing the separator (Figure 6c). The SEM image reveals the well-organized morphology of ZnO NWs on CNF mat (Figure 6d). The CNF matrix accelerates the electron transfer and ZnO NWs effectively improve the trapping and reutilization of active materials. High reversible capacity of 1030.7 mAh g<sup>-1</sup> was obtained at 0.2 C with 95% capacity retention after 50 cycles (Figure 6e).

Researchers have also utilized other metal oxides, such as  $\text{WO}_3$ ,<sup>[112]</sup>  $\text{SnO}_2$ ,<sup>[113]</sup> and  $\text{V}_2\text{O}_5$ ,<sup>[114–116]</sup> to form hybrid structures for the interlayer design. A report on  $\text{V}_2\text{O}_5$  presents the design of a mechanically sturdy, free-standing hybrid interlayer (GSVm) from 1D  $\text{V}_2\text{O}_5$  NWs and graphene nanoscrolls (GNSs).<sup>[114]</sup> The crosslinked 3D network provides highly conductive channels for ion/electron transfer and acts as a redox mediator which concurrently suppresses the polysulfide diffusion and accelerates their redox conversion via intermediate polythionate complex formation. The cell with a GSm (fluffy GNS film) interlayer presents a high discharge capacity of 938 mAh g<sup>-1</sup> compared to the GSVm-based one (812 mAh g<sup>-1</sup>); however, it doesn't sustain after 140 cycles at 0.5 C (Figure 6f,g). GSm provides only a physical barrier, insufficient for the stable confinement of soluble LiPSs over long-time cycling, whereas GSVm-based cell with high sulfur loading (5.5 mg cm<sup>-2</sup>) demonstrates a stable cyclic stability for 1000 cycles (Figure 6g). The LiPS adsorption capability of different interlayers was also verified by the UV-Vis measurements (Figure 6h), which endorses the higher affinity of GSVm toward liquid LiPSs.

Polar TMNs are also employed for the construction of functional interlayers due to their high electronic conductivity. For example, Kim et al.<sup>[117]</sup> designed a multifunctional interlayer on commercial PP separator with N-doped carbon embedded 1D TiN NWs (NC/TiN NWs@PP). Highly conductive polar TiN NWs show strong affinity toward LiPSs, which is further assisted by the polar sites emerged from the surrounding N-doped carbon

network. The presence of CNTs in the interlayer design provides additional conductive pathways which can simultaneously promote the redox conversion of LiPSs (Figure 6i). Comparison of rate performances of cells integrating different interlayers is shown in Figure 6j. This demonstrates a considerable improvement in the electrochemical kinetics of LSBs at high current densities, initially by introducing 1D TiN NW structure (TiN NW@PP) and subsequently by incorporating a N-doped carbon-embedded TiN NW network (NC/TiN NWs@PP). The finding was also corroborated by the voltage hysteresis data (Figure 6k).

Wang et al.<sup>[115]</sup> developed a free-standing, electronically conducting, multifunctional interlayer based on vanadium nitride NWs (VN-NWs), to simultaneously inhibit LiPS shuttling, promote lithium-ion migration, catalyze sulfur conversions, and improve adequate utilization of the active materials. Due to high catalytic activity and conductivity of VN, its combination with  $\text{V}_2\text{O}_3$  holds promise for application in the interlayer of LSBs. However, inorganic NWs with high surface energy have a higher tendency of agglomeration, which aggravate the situation of volume fluctuation. To subdue these, Zhao et al.<sup>[116]</sup> developed a porous free-standing interlayer, uniformly embedding hybrid  $\text{V}_2\text{O}_3/\text{VN}$  NWs into a carbonized bacterial cellulose (CBC) nanofiber network on commercial PP separator, to synergistically improve the sulfur utilization and rate performance and also buffer volume fluctuation (Figure 6l). GCD profiles (at 0.1 C) present lowest voltage hysteresis ( $\Delta E$ ) value and longest plateau for  $\text{V}_2\text{O}_3/\text{VN}/\text{C}$  interlayer, indicating efficient reutilization of soluble LiPSs and high specific discharge capacity for the corresponding cell (Figure 6m). The synergistic effect of  $\text{V}_2\text{O}_3$  and CBC can efficiently increase the discharge capacity, whereas inclusion of VN further enhances the kinetics of catalytic activity and long-term stability (Figure 6n).

Jung's group<sup>[118]</sup> designed a light-weight ( $\approx$ 0.43 mg cm<sup>-2</sup>) hybrid aerofilm interlayer (HAI), incorporating sulfonated tetrafluoroethylene (S-PTFE) and tunnel-structured  $\text{MnO}_2$  NWs. The sulfophilic  $\text{SO}_3^-$  groups of S-PTFE immobilize the LiPSs on its surface through chemical bonding and the  $\text{MnO}_2$  NWs promote the catalytic reactions. Besides suppressing the shuttle effect, it also facilitates the lithium-ion conduction through the interface (Figure 6o). Rate performance plot of HAI-based cell was significantly better than the cells using other interlayers (Figure 6p). Deconvolution of higher-order and lower-order polysulfide (HOPS, LOPS) contributions reveals that HAI interlayer efficiently prevents polysulfide shuttling and delivers high capacities at both upper and lower discharge plateaus, even at high C-rates, through effective LiPS conversion. Additionally, it facilitates catalytic conversion with a low overpotential during GCD (Figure 6q).

A flexible, multifunctional interlayer, consisting of a uniform film of super-aligned  $\text{Bi}_2\text{O}_3$ -polyoxometalate sub-1 nm NWs (SPMB SNWs film), was developed via a simple wet spinning method.<sup>[119]</sup> Highly ordered, multicomponent NW architecture not only improved sulfur redox conversions and ionic/electronic conductivity, but also stabilized the lithium anode up to a certain level. Li et al.<sup>[120]</sup> developed a 3D biocompatible interlayer (HNAP), by coating a composite of hydroxyapatite ( $\text{Ca}_5(\text{PO}_4)_3(\text{OH})$ ) NWs (HNS) and MWCNTs on conductive aramid fiber paper (AP). Due to the presence of polar bonds like -OH and P=O, HNs

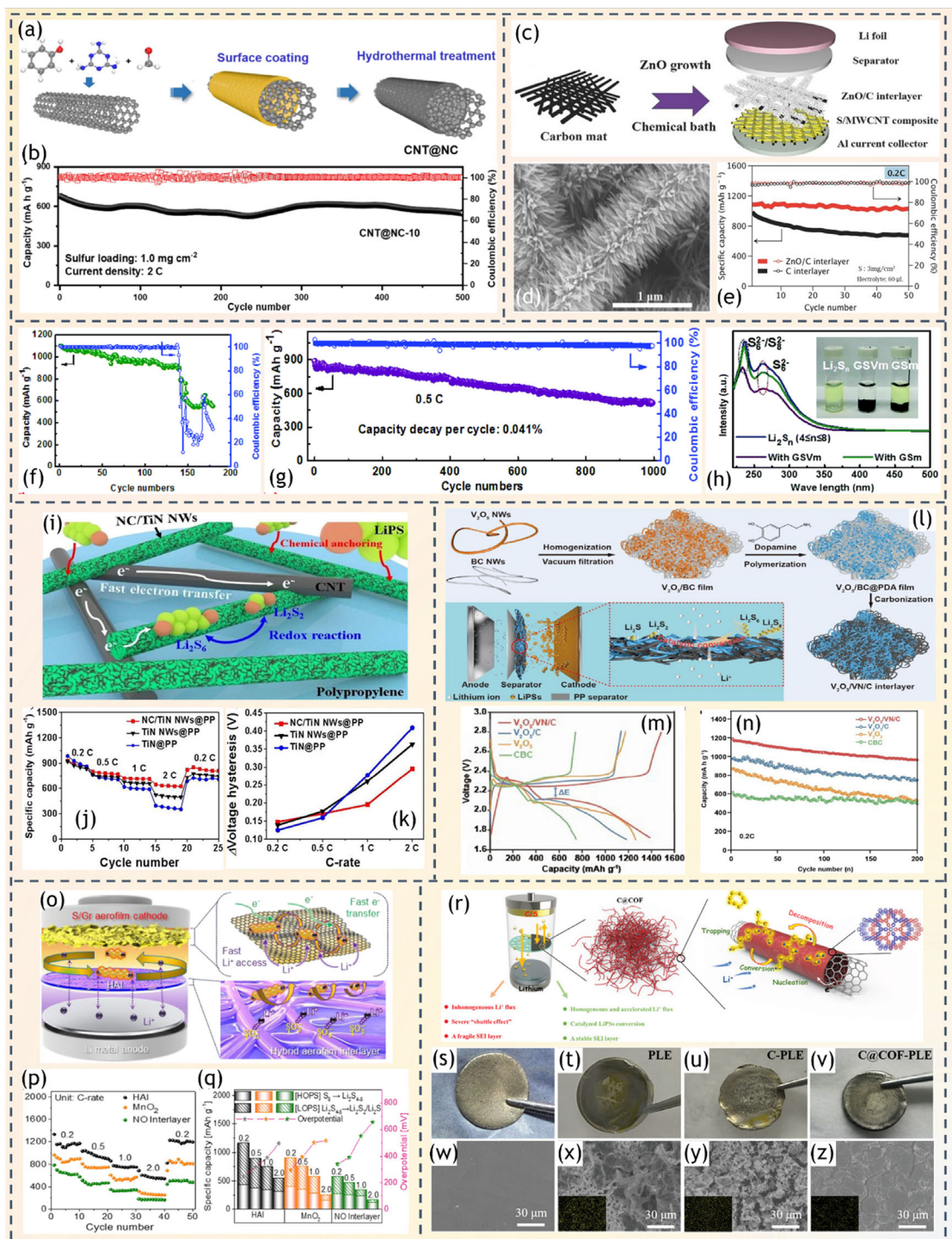


**Figure 6.** a) Schematic representation of synthesis of CNT@NC; b) long-term cycling of LSBs with CNT@NC-10 interlayer at 2 C. Reproduced with permission.<sup>[110]</sup> Copyright 2023, Elsevier. c) Illustration of the ZnO NW growth on carbon matrix and a LSB structure with resulting interlayer; d) SEM image of ZnO NWs/C interlayer; e) cyclic performance of LSBs with different interlayers. Reproduced with permission.<sup>[111]</sup> Copyright 2016, Wiley. Cycling of the LSB cells at 0.5 C using f) GSm and g) GSvM interlayers; h) UV-Vis absorption spectra of LiPS solutions at different conditions with digital photographs (inset). Reproduced with permission.<sup>[114]</sup> Copyright 2018, Royal Society of Chemistry. i) Mechanistic depiction of LiPS trapping and its conversion activity on NC/TIN NWs@PP plane; j) rate capability plots for LSBs using various separators; k) voltage hysteresis between GCD plateaus at different C-rates. Reproduced with permission.<sup>[117]</sup> Copyright 2021, Elsevier. l) Schematic illustration of  $\text{V}_2\text{O}_3/\text{VN}/\text{C}$  interlayer fabrication and its catalytic activity in an LSB module; m) GCD profiles and corresponding n) cyclic stabilities of LSB cells at 0.2 C using different interlayers. Reproduced with permission.<sup>[116]</sup> Copyright 2022, Elsevier. o) Pictorial overview of the lightweight LSB with sulfur/graphene cathode and HAI, and the catalytic mechanism of HAI and  $\text{MnO}_2$ ; p) comparison of rate performances of LSBs using different interlayers; q) deconvolution of HOPS and LOPS contributions in specific capacities, along with overpotentials calculated from the 10th GCD cycle. Reproduced with permission.<sup>[118]</sup> Copyright 2022, Elsevier. r) Infographic presents LSB mechanism without and with  $\text{C}@\text{COF}$ -based interlayer; photos of lithium anodes in LSBs without and with different interlayers; s) before and t-v) after 100 cycles at 1 C; corresponding w-z) SEM images and x-z) elemental sulfur mapping of the lithium surface. Reproduced with permission.<sup>[121]</sup> Copyright 2022, Wiley.

interact strongly with LiPSs through coordination bonds. The thermal and structural stability of the design make it more useful as an interlayer for wide range operations.

A simple sonochemical method was used to design a hierarchical porous interlayer by introducing a boroxine-based covalent organic framework (COF) onto a conductive CNT matrix (C@COF).<sup>[121]</sup> The COF features sulfophilic B sites as well as lithiophilic O sites which simultaneously immobilize the LiPSs (Figure 6r). The difference in the work functions between COF and CNT generates an interfacial electric field which also improves the charge transport and LiPS adsorption. The conductive backbone provides electrons to the outer COF structure and accelerates the conversions of adsorbed polysulfides. The core-shell design also expedites  $\text{Li}_2\text{S}$  decomposition during charging. The post-mortem analyses on the decrimped cells suggested that the lithium anode of the cell equipped with C@COF interlayer possesses the smoothest surface with lowest sulfur content, as evident through the digital photographs, SEM images, and elemental sulfur mapping (Figure 6s–z). Therefore, by designing a CNT/COF-based core-shell catalyst, the work offers new insights into the development of multifunctional materials for practical use of LSBs.

All these results clearly underline that achieving high capacity, excellent CE, and stable cyclic performance in LSBs rely on several features of modified separators and interlayers: high electrical conductivity, enhanced lithium-ion transport, strong chemical interactions with LiPSs, and effective catalytic activity for redox reactions. However, it is also important to manage the mass and volume of inactive components such as binders, in the interlayers and modified separators, as they can negatively impact the battery's overall energy density. Therefore, along with morphology and functionality control, optimizing the proportion of the constituent materials, as well as fine-tuning the thickness and porosity of modified separators and hybrid interlayers, is essential to maintain high energy density while improving performances. (Table 2) summarizes the details of separator/interlayer designs and corresponding electrochemical metrics of LSBs.

## 5. Computational Perspectives of Catalytic Mechanism

To have a fundamental understanding of the interactions between the sulfur electrocatalysts and the polysulfides at the molecular level, computational approaches have become a very powerful tool.<sup>[122–124]</sup> Density functional theory (DFT) calculations provide critical information on the interfacial binding energies for polysulfide adsorption. Density of states (DOS) calculation and relevant electronic structure determination help to probe the fundamentals of catalytic activities of the involved species. Additionally, transition state theory is used to calculate the reaction energy barriers between the active material and LiPSs, which helps explaining different electrochemical performances. Gibbs free energy calculations map the sulfur redox pathways and determine the speed of the electrochemical reactions.<sup>[122]</sup>

In the previous sections, we have discussed various heteroatom-doped carbonaceous NWs along with transition metal-based NWs based on oxides, sulfides, selenides, carbides, phosphides, nitrides, etc., which emerged as effective sulfur hosts and redox catalysts in LSBs. Their rich electronic structures and adsorption affinity toward LiPSs enable them to suppress shuttle effect while accelerating redox kinetics. Theoretical calculations are widely used to probe these features.<sup>[123]</sup> This section gives an overview of these intriguing chemistries from a DFT perspective. However, these static calculations based on DFT can't provide dynamic information on the reactions, while ab initio molecular dynamics (AIMD) simulations extend DFT calculations to simulate bond breaking, diffusion, and other interfacial phenomena in real time.<sup>[122]</sup> Overall, these computational tools provide mechanistic insights for the rational development of novel materials for LSBs with enhanced ability of polysulfide immobilization, catalytic conversion, and stable performance.

Wang et al.<sup>[56]</sup> used DFT calculations to interpret the interactions between LiPSs and (002) surface of  $\text{WO}_3$  hosts. Optimized binding geometries and corresponding adsorption energies are presented in Figure 7a. The results indicate that the  $\text{S}_8$  molecules stay flat on  $\text{WO}_3$  surface, whereas LiPS species strongly interact with  $\text{WO}_3$  (002) facets through Li–O bonds. During the adsorption and redox conversion processes,  $\text{Li}_2\text{S}_8$  and  $\text{Li}_2\text{S}_6$  encounter Li–S bond breakage, while S–S bonds stretch in  $\text{Li}_2\text{S}_2$  and  $\text{Li}_2\text{S}$  from 2.23 and 2.09 to 2.68 and 2.34 Å. Along with experimental data, these results further corroborate the immobilization of soluble sulfur species on  $\text{WO}_3$  surface and their subsequent conversions during repeated GCD cycles.

To explore the electronic structure of  $\text{Ni}_2\text{Co}_4\text{P}_3$  and understand the underlying catalytic processes, Shen et al.<sup>[78]</sup> conducted first principle DFT studies on hexagonal atomic model of  $\text{Ni}_2\text{Co}_4\text{P}_3$  (Figure 7b). Projected DOS (Figure 7c) features that the Co 3d band in  $\text{Ni}_2\text{Co}_4\text{P}_3$  lies higher than Ni 3d bands in both  $\text{Ni}_2\text{Co}_4\text{P}_3$  and  $\text{Ni}_2\text{P}$ . With lower d-band filling and higher d-band position of Co 3d than Ni 3d in  $\text{Ni}_2\text{Co}_4\text{P}_3$ , it permits stronger adsorption of polysulfide molecules than  $\text{Ni}_2\text{P}$ . Calculated binding energies (Figure 7d) indicate that  $\text{Li}_2\text{S}_4$  has selectively stronger adsorption on (110) facets of both  $\text{Ni}_2\text{P}$  and  $\text{Ni}_2\text{Co}_4\text{P}_3$ . Figure 7e displays the optimized binding geometry of  $\text{Li}_2\text{S}_4$  on  $\text{Ni}_2\text{P}$  and  $\text{Ni}_2\text{Co}_4\text{P}_3$  surface. Presence of shorter metal–S bonds and elongated S–S bonds on  $\text{Ni}_2\text{Co}_4\text{P}_3$  confirms strong adsorption and facile conversion of LiPSs. Crystal orbit overlap population (COOP) analysis (Figure 7f) reflects higher electron occupancy in the antibonding states of terminal S1–S2 and S3–S4 bonds for  $\text{Li}_2\text{S}_4$  on  $\text{Ni}_2\text{Co}_4\text{P}_3$  than on  $\text{Ni}_2\text{P}$ . In addition, the energy required to break the S–S bonds significantly drops due to interactions between  $\text{Li}_2\text{S}_4$  and  $\text{Ni}_2\text{Co}_4\text{P}_3$ , indicating toward lower energy barrier for subsequent lithiation.

Zha et al.<sup>[83]</sup> employed a double layer adsorption model for DFT calculations on (200) facets of TiN sample, where sulfur atoms were first adsorbed onto the TiN (200) surface, followed by the introduction of LiPS molecules on top of the sulfur layer in different orientations. Adsorption energies corresponding to the second layer are shown in Figure 7g–k, where more negative value refers to stronger adsorption of LiPSs on the TiN surface. Stronger

**Table 2.** Overview of LSB performances with and without integrating modified separators or hybrid interlayers, featuring material types, sulfur contents, and electrochemical metrics.

Material	Separator/interlayer fabrication <sup>a)</sup>	Separator type <sup>a)</sup>	Mass loading of separator/interlayer [mg cm <sup>-2</sup> ]	Cathode <sup>a)</sup>	Sulfur loading [μL mg <sup>-1</sup> ]	Sulfur loading E/S [mg cm <sup>-2</sup> and E/S]	Electrochemical metrics		Without capacity [mAh g <sup>-1</sup> ]	Reference
							Cyclic stability (C rate)	Retained capacity [mAh g <sup>-1</sup> ]		
<i>Modified separators</i>										
N-PNW	TM, CM, TA & SC	CG	0.4	S	1.5–1.7 & -	500 (0.5)	507.6	177.7	[104]	
MnO <sub>2</sub> /CNT	HT, US & VF	CG 2500 (PP)	0.35	S/PC	0.8 & 20	100 (0.5)	670.9	371.8	[102]	
Co-MnO/NCNFs	ST, TA & SC	CG 2500 (PP)	1	C/S	1.5–4.2 & -	800 (1)	634	≈275 (aft. 415 cyc.)	[105]	
STO-W/S	HT, TA & VF	CG 2325 (PP)	-	AC/S	0.8–1 & 20	500 (1)	541.4	-	[106]	
VOH@PANI	SG, PM & VF	CG 2500 (PP)	0.2	CB/S	1.2–6.5 & 12–20	1000 (1)	585.8	323	[103]	
PPy NW	TM, PM & VF	CG 2320	1	S/KB	2.5–3 & -	200 (0.2)	832.1	215	[135]	
NC-Ti <sub>0.95</sub> Co <sub>0.05</sub> N	ES, NT & SC	CG 2400 (PP)	0.7–0.8	S/SP	1.2–3.6 & 10–25	200 (0.1)	464.4	400	[107]	
InN NW	NT & SC	-	0.3	S	1.5–6 & 5–40	1000 (1)	634.6	103.4	[108]	
<i>Hybrid interlayers</i>										
CNT@NC	PC, TA & SC	CG 2500 (PP)	-	KB/S	1–5 & -	500 (2)	550	-	[110]	
ZnO/C	ES, TA & CBD	PP	1.3	S/MW/CNT	3–5.2 & -	200 (1)	776	-	[111]	
WNW/CNT	HT, US & VF	CG 2400 (PP)	2 (typical)	S	1.5–5.3 & 20	300 (0.5)	836.6	-	[112]	
SnO <sub>2</sub> NWs@CP	CVD	CG 2400 (PP)	0.4–2.5	S	2.2–7.1 & -	100 (0.2)	886	520	[113]	
G5Vm	HT, CM, US & VF	CG 2400	0.642	S	1.5–5.5 & -	1000 (0.5)	516	≈330 (aft. 100 cyc.)	[114]	
NC/TiN NWs	ES, NT & VF	CG 2400 (PP)	1.1	S/KB	1.6–5.9 & -	150 (0.2)	720	≈470 (aft. 140 cyc.)	[117]	
VN NWs	HT, NT & VF	CG 2400	-	S	1.9–5.5 & 15	300 (0.5)	878	≈500 (aft. 100 cyc.)	[115]	
V <sub>2</sub> O <sub>3</sub> /VN/C	HT, CM, VF & TA	PP	-	S	0.9–1.1 & -	1000 (1)	768.7	-	[116]	
HAI	HT & IF	CG 2500 (PP)	≈0.43	S/G aerofilm	4.3–4.7 & 5–46	500 (0.2)	1189	177	[118]	
S-PMB SNWs	WS	PP	-	S	1.5–9.6 & -	850 (2)	782	≈360	[119]	
HNAP	HT & SC	CG 2300	-	S	1.53 & -	200 (1)	840	-	[120]	
C@COF	US & VF	CG 2400 (PP)	0.4	S/CNT	1.2–6.8 & -	500 (1)	655.7	277.7	[121]	

<sup>a)</sup>Note: Abbreviations for some frequently used terms below—template method (TM), chemical mixing (CM), thermal annealing (TA), slurry coating (SC), Celgard (CG), sulfur powder (S), hydrothermal (HT), ultrasonication (US), vacuum filtration (VF), polypropylene (PP), porous carbon (PC), solvothermal (ST), carbon (C), activated carbon (AC), sol-gel method (SG), polymerization (PM), carbon black (CB), Ketjenblack (KB), electrospinning (ES), nitridation (NT), super P (SP), polymer coating (PC), chemical bath deposition (CBD), graphene (G), infiltration (IF), wet-spinning (WS).

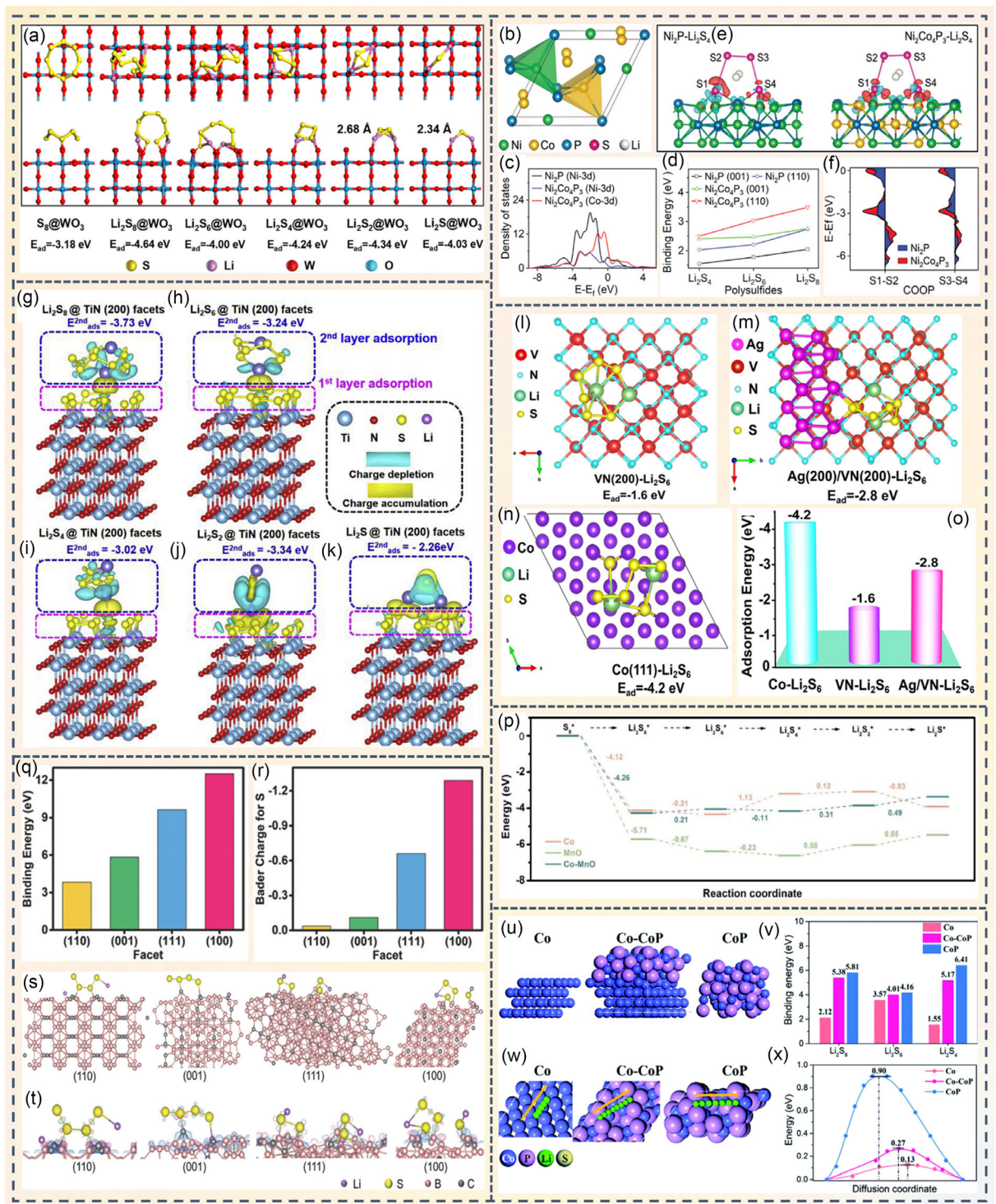


**Figure 7.** a) Optimized configurations and corresponding adsorption energies of different LiPS species on (002) surface of  $\text{WO}_3$ . Reproduced with permission.<sup>[56]</sup> Copyright 2025, Royal Society of Chemistry. b) atomic model of hexagonal  $\text{Ni}_2\text{Co}_4\text{P}_3$  structure; c) calculated DOS and d) binding energies of different LiPS species on different facets of  $\text{Ni}_2\text{P}$  and  $\text{Ni}_2\text{Co}_4\text{P}_3$ ; e) optimized adsorption geometries for  $\text{Li}_2\text{S}_4$  on  $\text{Ni}_2\text{P}$  and  $\text{Ni}_2\text{Co}_4\text{P}_3$  and f) corresponding COOP diagram for S1-S2 and S3-S4 bonds of  $\text{Li}_2\text{S}_4$ . Reproduced with permission.<sup>[78]</sup> Copyright 2020, Wiley. g-k) Side view of charge density differences for most favorable adsorption configurations of different polysulfides on  $\text{TiN}(200)$  surfaces. Reproduced with permission.<sup>[83]</sup> Copyright 2020, Elsevier. l-o) Top view with  $\text{Li}_2\text{S}_6$  molecule on top of  $\text{VN}(200)$ ,  $\text{Ag}(200)/\text{VN}(200)$ , and  $\text{Co}(111)$  facets; comparison of  $\text{Li}_2\text{S}_6$  binding energies on these surfaces. Reproduced with permission.<sup>[86]</sup> Copyright 2021, American Chemical Society. p) Gibbs free energy calculations for the electrochemical reductions of sulfur and LiPS intermediates on Co,  $\text{MnO}$ , and Co-MnO surfaces. Reproduced with permission.<sup>[105]</sup> Copyright 2023, Elsevier. q) calculated binding energies and r) Bader charges for sulfur atoms at different facets of  $\text{B}_4\text{C}@\text{CNT}$  structure; s) optimized binding model of  $\text{Li}_2\text{S}_4$  on  $\text{B}_4\text{C}$  facets and t) corresponding charge distributions on these surfaces during  $\text{Li}_2\text{S}_4$  adsorption. Reproduced with permission.<sup>[90]</sup> Copyright 2018, Wiley. u) Stable atomic models of Co, Co-CoP, and CoP; v) optimized binding energies between LiPSs and electrode surfaces; w) Li-ion migration pathways and x) corresponding ion diffusion energies on these materials with marked diffusion barriers. Reproduced with permission.<sup>[77]</sup> Copyright 2021, Royal Society of Chemistry.

adsorption is primarily attributed to the lower coordinated Ti sites (5 coordinated Ti sites,  $Ti_{5c}$ ) on TiN (200) surface.  $Ti_{5c}$  sites form stable Ti–S covalent bonds to effectively anchor soluble LiPSs, which becomes more evident from the comparative studies performed on common TiN (220) facets.

Zhan's group<sup>[86]</sup> carried out DFT calculations to probe the interactions between LiPSs and Ag/VN@Co/NCNT structure. The study was performed on VN (200), Ag (200)/VN (200) heterostructure, and Co (111) models. Favorable binding configurations of  $Li_2S_6$  on these surfaces are presented in Figure 7l–n. Corresponding adsorption energies (Figure 7o) show that Ag/VN structure has lower adsorption energy than pristine VN surface, facilitating stronger LiPS adsorption, while Co shows lowest adsorption energy.

In another article incorporating Co and NCNTs, Yu et al.<sup>[105]</sup> demonstrated a hybrid heterostructure of Co-MnO significantly boosts sulfur redox processes through synergistic adsorption, diffusion, and conversion processes. Theoretical calculations show that incorporation of Co atoms in MnO simultaneously increases DOS at the Fermi levels and induces built-in electric field at the interface, thereby enhancing electronic conductivity of the material along with facilitating fast charge migration during charging/discharging. Figure 7p presents the Gibbs free energy evolution along sulfur reduction pathways on Co, MnO, and Co-MnO heterointerface. Conversion of  $Li_2S_6$  to  $Li_2S_4$  on Co surface leads to a positive Gibbs free energy value, while the formation of  $Li_2S$  on MnO surface from  $Li_2S_4$  and  $Li_2S_2$  is thermodynamically unfavorable. However, in comparison to MnO, Co-MnO architecture significantly reduces the energy barriers toward final  $Li_2S$  nucleation, making the whole sulfur reduction process favorable with enhanced reaction kinetics. In a related article,<sup>[125]</sup> Gibbs free energy calculations for LiPS reduction were performed on Co, Co– $Co_3O_4$ , and  $Co_3O_4$  surfaces, where pristine  $Co_3O_4$  showed higher affinity toward LiPSs, which detrimentally affected the structure and subsequent catalytic processes of LiPSs. However, after combining Co with  $Co_3O_4$ , the binding energies reached an optimal range, which ensured suitable LiPS anchoring without affecting further conversions.

In 2018, Manthiram's group<sup>[90]</sup> investigated  $Li_2S_4$  adsorption capability of  $B_4C$ @CNF NWs by simulating the binding geometries using different facets of  $B_4C$  (Figure 7q–t). Theoretical calculations confirmed that  $B_4C$  had remarkably higher binding energies (3.84–12.51 eV), surpassing the reported transition metal chalcogenides (3.5–7.0 eV) (Figure 7q). The adsorption strength strongly depends on the presence of particular bonds in the respective crystallographic planes; particularly, S–B bonds lead to higher binding energies than S–C bonds. Bader charge analyses (Figure 7r) show significant electron transfer between  $Li_2S_4$  and  $B_4C$ , consistent with the binding energy data. Charge density difference plots in Figure 7t show the distribution of accumulated charges in  $Li_2S_4$ – $B_4C$  system, further confirming the robust anchoring of  $Li_2S_4$  on  $B_4C$  facets.

Li et al.<sup>[77]</sup> used spin-polarized DFT calculations for Co, Co-CoP, and CoP atomic models (Figure 7u) to fully understand the characteristics of Co 3d electrons in these structures and demonstrate the origin of LiPS trapping and Li-ion diffusion in Co-CoP

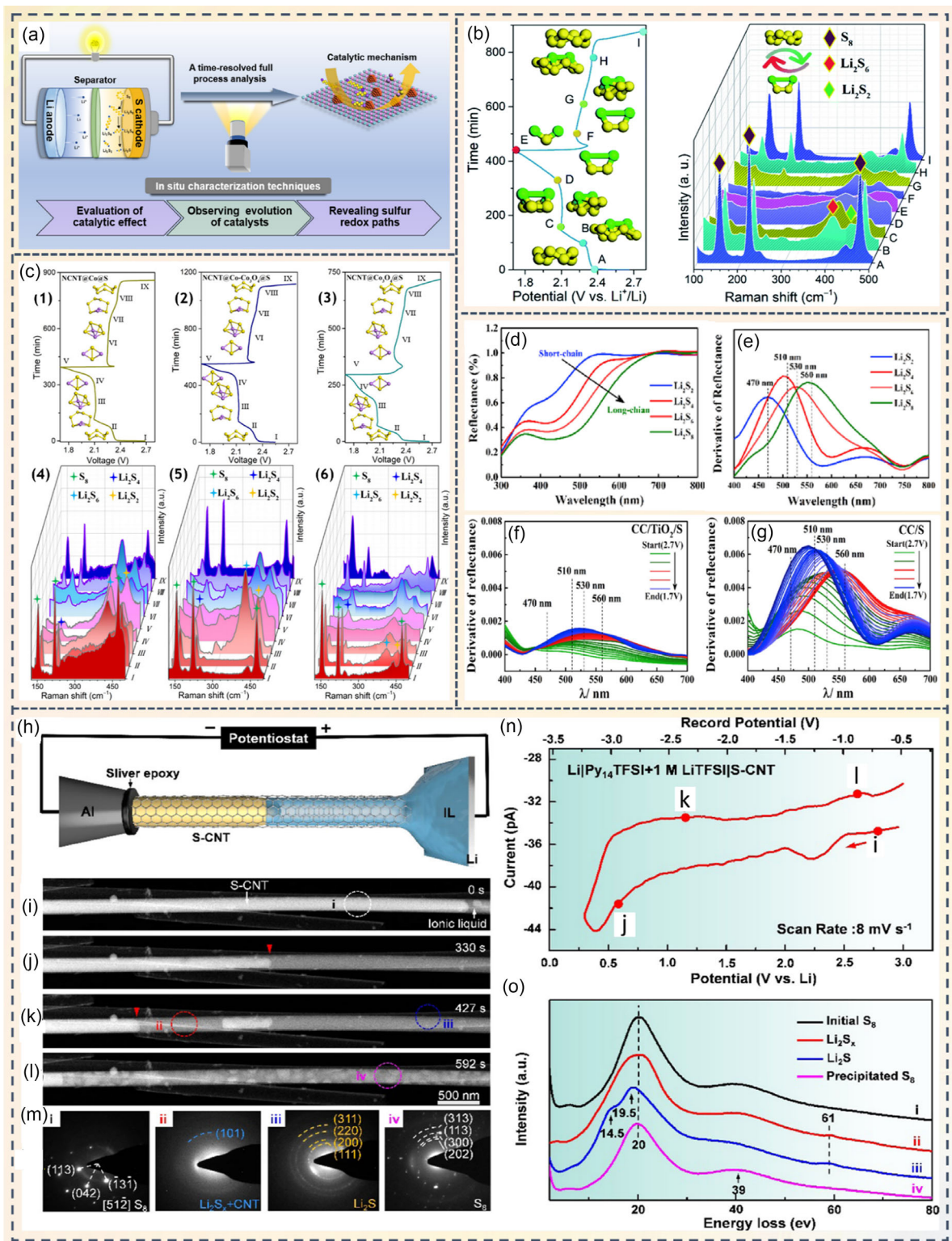
heterointerface. Binding energy calculations on (111) facets of Co and CoP show Co-CoP has the optimum affinity toward LiPSs (Figure 7v), compared to lower and higher binding energies for Co and CoP respectively. This moderate binding strength matches well with the Sabatier's principle, ensuring proper LiPS anchoring and subsequent conversions. Additionally, redox kinetics were studied by examining Li-ion diffusion behavior (Figure 7w,x). Obtained diffusion barrier values (Figure 7x) further confirm that Co-CoP heterostructure provides a moderate barrier for ion migration, efficiently promoting Li-ion diffusion and sulfur redox reactions.

Therefore, DFT studies provide critical information on polysulfide adsorption mechanisms and catalytic activities along with important insights on electronic structures for rational material design. However, DFT can't simulate actual battery conditions considering electrolyte effects, surface charge generation, and material degradation. Recent development in high-end computation techniques and machine learning (ML) approaches can complement DFT studies and lead LSB research toward further development.

## 6. *In Situ* Characterization Techniques

Over the past decades, the key challenges of LSBs have been extensively investigated, with a major emphasis on the rational design of functional electrocatalysts. As discussed previously, a diverse range of materials has been developed and implemented in different components of LSBs, with the primary aim of mitigating the key challenges.<sup>[126,127]</sup> However, efficient catalyst design predominantly depends on rigorous understanding of the electrochemical processes associated with the evolution of multiple intermediate sulfur species and identifying the active catalytic sites. Several factors hinder the clear understanding of the catalytic mechanisms in LSBs. The stepwise sulfur conversions during battery cycling often remain elusive and sometimes polysulfide conversion is hypothesized to have connection with intermediate product formation on the surface of the catalysts. Another inevitable limitation originates from the catalyst's susceptibility to degradation and deactivation. Furthermore, the catalyst's influence on the microstructure and spatial arrangement of sulfur species at the electrode/electrolyte interface becomes another crucial factor and needs thorough inspection to optimize LSB performance. Therefore, a comprehensive understanding of the whole catalytic process is crucial and requires thorough investigation using multiple advanced imaging and spectroscopic characterization techniques.<sup>[128]</sup>

In recent years, the rapid development of state-of-the-art *in situ* characterization techniques has significantly improved the understanding of catalytic mechanism of LSBs (Figure 8a).<sup>[128,129]</sup> *In situ* techniques offer several key advantages over *ex situ* techniques such as (a) continuous tracking of reaction coordinates throughout the electrochemical processes, (b) ability to perceive spatially resolved information of the catalyst's surface caused by the minor modulation of local structure and electronic environment, and (c) having qualitative and quantitative information about the



interaction between catalytic centers and the reactants during the reaction. Overall, these features provide powerful insights in real time to fundamentally understand the correlation between the catalyst's performance and step-wise evolution of sulfur species, offering a more comprehensive understanding about LSB mechanism.

In the following section, we will discuss a few reports where *in situ* spectroscopic and microscopic characterization techniques have been effectively employed for probing the NW-based electrocatalysts in LSBs. *In situ* Raman spectroscopy can detect various forms of sulfur intermediates and other discharge byproducts qualitatively and semi-quantitatively, depending on the state-of-charge of the cell. In addition, it can determine the equilibrium between the different polysulfide phases and reappearance of solid sulfur during charging.<sup>[130]</sup> Shao and his group<sup>[77]</sup> conducted *in situ* Raman spectroscopy measurement on LSB cells using NCNT@Co-CoP NW cathode to understand the adsorption and catalytic conversions of LiPSs on the designed hierarchical cathode with very high sulfur loading of  $10 \text{ mg cm}^{-2}$  and low E/S ratio of 7. Figure 8b presents the voltage-time profile for the battery module at 0.1 C and the corresponding *in situ* Raman spectra. Point A denotes the initial state of the battery, with characteristic Raman peaks of solid sulfur ( $S_8$ ) at 150, 219, and  $474 \text{ cm}^{-1}$ . Upon discharging (point B),  $S_8$  peaks gradually weaken as new peaks evolve for  $\text{Li}_2\text{S}_6$  ( $398 \text{ cm}^{-1}$ ) and  $\text{Li}_2\text{S}_2$  ( $452 \text{ cm}^{-1}$ ). At points C and D,  $S_8$  peaks completely vanish as it converts to  $\text{Li}_2\text{S}_6$  and  $\text{Li}_2\text{S}_2$ . At point E ( $\approx 1.70 \text{ V}$ ), only  $\text{Li}_2\text{S}_2$  peak remains, indicating complete conversion of intermediate polysulfides to  $\text{Li}_2\text{S}_2$  on NCNT@Co-CoP-1 NW-based cathode. During charging, reverse transformations take place (point F to I), converting  $\text{Li}_2\text{S}_2$  to  $\text{Li}_2\text{S}_6$  and gradually back to  $S_8$  (point I,  $\approx 2.80 \text{ V}$ ). Reappearance of the Raman peaks related to  $S_8$  restoration indicates toward the excellent reversibility of the cell. In a related study,<sup>[125]</sup> *in situ* Raman technique was employed to investigate adsorption and conversion efficiency of LiPS on nitrogen-doped carbon nanotube-supported Co– $\text{Co}_3\text{O}_4$  (NCNT@Co– $\text{Co}_3\text{O}_4$ ) NW arrays (NWAs) cathode, during GCD at 0.1 C (Figure 8c). Initially at 2.4 V (point I) the  $S_8$  peaks are visible for all electrodes. Upon discharge till 2.1 V (point III),  $S_8$  peaks in NCNT@Co– $\text{Co}_3\text{O}_4$  cathode completely disappear. Other new peaks slowly appear at 398, 202, and  $452 \text{ cm}^{-1}$ , corresponding to  $\text{Li}_2\text{S}_6$ ,  $\text{Li}_2\text{S}_4$ , and  $\text{Li}_2\text{S}_2$  respectively. Continued discharge leads to a dominant peak for  $\text{Li}_2\text{S}_2$  (point IV), with that of long-chain LiPS species ( $\text{Li}_2\text{S}_6$  and  $\text{Li}_2\text{S}_4$ ) inevitably vanishing at point V. During charging, the redox processes trace back the discharge path, regenerating  $S_8$  at 2.8 V (point IX). Unlike NCNT@Co– $\text{Co}_3\text{O}_4$ , NCNT@Co@S and NCNT@ $\text{Co}_3\text{O}_4$ @S-based cathodes show incomplete LiPS conversion efficiencies with slow kinetics and severe shuttle effect, as manifested by the Raman measurements. Despite the usefulness of *in situ* Raman technique, signals from most of the intermediate LiPS species are inherently weak, limiting its broad application in LSBs. Enhancing sensitivity and precision through surface-enhanced Raman spectroscopy or shell-isolated nanoparticle-enhanced Raman spectroscopy could improve effective implementation of Raman spectroscopy, for having valuable insights into complex electrochemistry.<sup>[129]</sup>

Another useful *in situ* characterization technique, UV-Vis spectroscopy, has been widely used in LSBs. It provides qualitative and quantitative information on the dynamic evolution of LiPSs by tracking the real-time absorbance of the colorful soluble polysulfides during cell cycling.<sup>[131]</sup> Yan et al.<sup>[64]</sup> implemented this technique to probe a 3D binder-free cathode, constructed from *in situ* grown polar  $\text{TiO}_2$  NWs on a carbon cloth (CC/ $\text{TiO}_2$ ), for LSB system. This design offers high surface area and excellent electronic conductivity, significantly improving the polysulfide adsorption, redox conversion kinetics, and shuttle effect. Reflectance spectra (Figure 8d) of different standard polysulfide species ( $\text{Li}_2\text{S}_2$ ,  $\text{Li}_2\text{S}_4$ ,  $\text{Li}_2\text{S}_6$  and  $\text{Li}_2\text{S}_8$ ) indicate that long-chain and short-chain LiPSs absorb at longer and shorter wavelengths respectively. The derivative peaks of reflectance spectra (Figure 8e) appear at 560, 530, 510, and  $470 \text{ nm}$  for  $\text{Li}_2\text{S}_8$ ,  $\text{Li}_2\text{S}_6$ ,  $\text{Li}_2\text{S}_4$ , and  $\text{Li}_2\text{S}_2$ , respectively. During discharge, both CC/ $\text{TiO}_2$ /S and CC/S cathode present a decrease in reflectance at higher wavelength due to the formation of long-chain polysulfides, apparent from the increased peak intensity in the first-order derivative profiles (Figure 8f,g). With further discharge of the cells, more peaks start to appear near to the shorter wavelengths, indicating the formation of mid-chain and short-chain polysulfides. CC/S cathode presents rapid change in reflectance spectra due to its poor LiPS adsorption efficiency, causing dissolution of intermediate polysulfides in the electrolyte. However, higher LiPS adsorption efficiency of CC/ $\text{TiO}_2$ /S leads to minimal change in the reflectance, indicating effective polysulfide retention during cycling. Overall, this cost-effective technique conveniently delivers critical insights into the LSB mechanism without compromising cell chemistry.

The *in situ* TEM setup integrated with electrochemical techniques effectively probes the kinetics of the different electrochemical reactions with high spatial and temporal resolutions. However, it becomes very challenging to image sulfur due to its inherent sensitivity toward high energy electron beam and high vacuum.<sup>[132]</sup> Most *in situ* TEM setups are almost of similar design with subtle variations in cell design. Wang et al.<sup>[133]</sup> developed an aberration-corrected *in situ* TEM imaging setup to study the polysulfide generation and sulfur/electrolyte interface in an ionic liquid (IL) electrolyte-based system. The electrochemical cell was configured with tip-flattened aluminum rod appended to a partially sulfur-filled CNT (S-CNT) cathode and a lithium metal anode, separated by an IL electrolyte (with/without lithium salts), allowing nanoscale imaging in real-time (Figure 8h). The encapsulated IL immediately formed an IL/S interface inside the half-filled S-CNT. Figure 8i–l show the structural evolution of the S-CNT cathode and movement of IL/S interface (red arrow). During discharge (Figure 8i–k), sulfur was reduced to soluble LiPSs, which subsequently reacted with lithium to generate insoluble  $\text{Li}_2\text{S}$  nanoparticles. However, sulfur nanoparticles start to emerge on the inner surface of CNT (Figure 8l), when the potential was scanned from 0.3 V to OCV (versus  $\text{Li}/\text{Li}^+$ ). The selected area electron diffraction (SAED) patterns (Figure 8m) from circled regions in Figure 8i,k,l identify the emergence of different sulfur species over time. The concurrent CV profile is shown in Figure 8n. Additionally, the low-loss spectra in EELS data (Figure 8o) further confirm sulfur dissolution, precipitation and

intermediate LiPS formation during redox conversions. In short, time-lapse *in situ* TEM imaging combined with these associated measurements unravels the real-time microstructure evolution and electrochemical sulfur conversion, offering critical insights into the complex electrochemistry of LSBs.

Although *in situ* characterization techniques have garnered considerable attention for providing a thorough understanding of the complex reaction mechanisms of LSBs, studies focusing on NW-based LSB systems remain relatively limited. There is substantial potential for employing advanced *in situ* characterization technique to further optimize and develop more efficient battery materials for LSBs.

## 7. Summary and Future Outlook

In recent years, there is a surge in the development of high-energy LSBs. However, the commercialization of LSBs has been severely hindered by some critical issues such as intrinsic low conductivity of sulfur, loss of active materials due to polysulfide shuttling, volume fluctuation during repetitive cycling, and surface passivation on anode. To tackle these cardinal issues, NW-based materials offer a plausible solution over bulk materials. This review outlines the key challenges of LSBs, followed by highlighting the importance of NW architectures in enhancing battery performances. It provides a rigorous discussion on the recent progress of integrating NW electrocatalysts in different LSB components, followed by a brief discussion on different *in situ* characterization techniques, used to probe these systems for unveiling the energy storage mechanism.

NWs provide a wide opportunity to develop intriguing hybrid, hierarchical architectures featuring cross-linked porous networks with interconnected conductive channels, which synergistically improve the structural stability and electrolyte infiltration through the structure, promoting electrochemical performance of LSBs. Despite promising lab-scale research, commercial viability is yet to be achieved. Challenges persist in terms of interfacial parasitic reactions due to high surface area; NW agglomeration during repetitive cycling, causing increased internal impedance and subsequent capacity degradation; and reduced electrical conductivity because of smaller electronic mean free path and expensive synthesis methods. Addressing these issues will be essential for unleashing the full potential of NWs in the LSB system. Moreover, there is an imperative urgency to comprehensively understand the fundamental electrochemistry for each system and the interaction of LiPS species with the active electrocatalysts. Advancement in this area requires a synergistic blend of computational studies and state-of-the-art experimental techniques. Despite persisting challenges, there is substantial room for improvement in NW-based LSBs, to propel the advancement toward practicality. So, before concluding, we would like to outline some ideas and future outlook, which may be useful to the researchers in this field:

1) Since the properties of NWs are highly reliant on their morphology and dimensions, development of efficient synthesis methods with precise control is essential. To ensure greater accuracy and reproducibility, it is imperative to develop novel

synthesis strategies with in-depth knowledge of the microscopic growth processes along with optimizing the existing techniques. This can be achieved through a combined interdisciplinary approach, employing chemistry for the selection of precursors and interpretation of reaction mechanisms, physics for controlling and understanding the effect of thermal/electric field during the growth of NWs, and material science for interface engineering and comprehending the surface chemistry. Such convergence could lead to the development of new, reliable, and scalable synthesis techniques for NWs.

2) Currently, most of the NW fabrication processes remain constrained to the lab-scale production and hardly meet the commercial viability due to less yield and high cost. Scalable production methods with desirable properties are still cumbersome and costly processes. The fabrication of NWs at industrial scale requires the development of large-scale synthesis techniques capable of continuous operation such as roll-to-roll electrospinning techniques, CVD, or electrodeposition in large baths, which can ensure the quality, structural integrity, and electrochemical performances during scale-up. Advancements in chemical processing methods, reactor design, and cost-efficient manufacturing technologies can bridge this gap between lab-scale research and commercial applications of NWs in LSBs.

3) Besides developing cutting-edge manufacturing techniques, it is also important to focus on the advancement of hierarchical porous NW structures to accommodate high areal sulfur loading and facilitate rapid ion migration. Additionally, NW-based sulfur hosts should be capable of tolerating  $\approx 80\%$  volume variations during charging/discharging without losing the structural integrity of the cathode. Rational design of core-shell NWs or flexible polymer-based NWs offers a promising approach toward the volume expansion concern. Furthermore, integrating NWs into 3D architectures such as foam, aerogel, or fiber mats can simultaneously maximize both electrical conductivity, structural stability, and active material utilization.

4) Theoretical and ML approaches are of paramount importance in accelerating material discovery and supporting experimental observations. First-principles calculations like DFT can predict host-polysulfide interactions and investigate the DOS near the Fermi level, determining contributions from particular atomic orbitals of the constituent elements. Artificial intelligence (AI) and ML tools are equally important for the development and optimization of futuristic battery materials. However, their applications in NW-based LSBs remain limited. Synergistic integration of the data from DFT, molecular dynamics (MD) simulations, and experimental studies into ML algorithms can significantly accelerate the discovery and optimization of novel materials. ML tools can predict material properties and interpret morphological variations as well. To date, these computational approaches are underexplored in NW-based LSB research. Consequently, this could be a promising and largely untapped opportunity for future exploration.

5) *In situ* characterization techniques hold significant potential for acquiring real-time information on the fundamental electrochemical processes of LSBs and critical understanding of the structural evolution of battery electrodes. Advanced *in situ* characterization techniques such as *in situ* XRD, X-ray absorption

spectroscopy (XAS), UV-Vis, FTIR, EIS, TEM, X-ray tomographic microscopes (XTM), and neutron depth profiling (NDP) can certainly enrich the scientific understanding by monitoring the sulfur conversions and dynamic morphological evolution of catalysts during cell operation. However, some *in situ* cell configurations fail to replicate real battery conditions, often requiring customized cell geometries for specific experimental objectives. Additionally, a major challenge remains in tracking the reactions when the reaction components are sensitive to the electron beam and high vacuum. Therefore, optimizing the cell designs and reaction conditions would be essential for accurate data interpretation and guiding a sustainable development of NW-based LSBs.

Finally, the remaining challenges and high prospects of NW-based materials will provide exciting opportunities to shape the evolution of LSB research field. Addressing each of the challenges with well-designed methodologies and targeted strategies would be crucial. In that context, we hope that this review will motivate researchers for further exploration in this field.

## Acknowledgements

A.D. and M.R.B. would like to acknowledge the support of the PN 23 15 02 01—BatNaS project, funding from the Romanian Ministry of Research, Innovation, and Digitalization. T.P.P., M.G.O., and J.M.P. acknowledge the funding by the European Union's Next Generation funds, coordinated at the Spanish level by the Recovery, Transformation and Resilience Plan, and included in the investment Complementary Plan of Energy and Renewable Hydrogen.

Open access publishing facilitated by Anelis Plus (the official name of "Asociatia Universitatilor, a Institutelor de Cercetare – Dezvoltare si a Bibliotecilor Centrale Universitare din Romania"), as part of the Wiley - Anelis Plus agreement.

## Conflict of Interest

The authors declare no conflict of interest.

## Author Contributions

**Tushar Prashant Pandit and Anweshi Dewan** conceived the idea, conducted the literature review, and equally contributed to the manuscript. **Mariela Gisela Ortiz, Juan M. Pérez, and Mihaela Ramona Buga** contributed to the manuscript's revision and editing. **Mihaela Ramona Buga** also assisted with funding acquisition.

**Keywords:** 1D nanowires • Li–S batteries • LiPS conversion • polysulfide immobilization • shuttle effect

- [1] *Batteries and Secure Energy Transitions IEA*, Paris 2024.
- [2] A. Dewan, S. Sur, R. Narayanan, M. O. Thotiyil, *ChemElectroChem* 2022, 9, e202200001.
- [3] A. Dewan, R. Narayanan, M. O. Thotiyil, *Nanoscale* 2022, 14, 17372.
- [4] S. Pal, X. Lin, P. Apostol, C. Ungureanu, D. Tie, V. R. Bakuru, D. Rambabu, N. Campagnol, A. Kachmar, C. Poleunis, G. Barozzino-Consiglio, M. Buga, A. Vlad, *ACS Energy Lett.* 2024, 9, 4399.
- [5] H. Yuan, W. Lin, C. Tian, M. Buga, T. Huang, A. Yu, *Nano-Micro Lett.* 2025, 17, 288.
- [6] T. Tite, C. Ungureanu, M. Buga, I. Stavarache, E. Matei, C. C. Negrila, L. Trupina, A. Spinu-Zalet, A. C. Galca, *J. Electroanal. Chem.* 2023, 933, 117290.
- [7] D. Versaci, R. Colombo, G. Montinaro, M. Buga, N. C. Felix, G. Evans, F. Bella, J. Amici, C. Francia, S. Bodoardo, *J. Power Sources* 2024, 613, 234955.
- [8] M.-R. Buga, A. A. Spinu-Zalet, C. G. Ungureanu, R.-A. Mitran, E. Vasile, M. Florea, F. Neatu, *Molecules* 2021, 26, 4531.
- [9] R. Azmi, F. Lindgren, K. Stokes-Rodriguez, M. Buga, C. Ungureanu, T. Gouveia, I. Christensen, S. Pal, A. Vlad, A. Ladam, K. Edström, M. Hahlén, *ACS Appl. Mater. Interfaces* 2024, 16, 34266.
- [10] B. Vedhanarayanan, K. C. Seetha Lakshmi, *Front. Batteries Electrochem.* 2024, 3, 1377192.
- [11] P. M. Tembo, C. Dyer, V. Subramanian, *NPG Asia Mater.* 2024, 16, 43.
- [12] S. Bandyopadhyay, B. Nandan, *Mater. Today Energy* 2023, 31, 101201.
- [13] H. Hong, N. A. R. C. Mohamad, K. Chae, F. M. Mota, D. H. Kim, *J. Mater. Chem. A* 2021, 9, 10012.
- [14] Y. Lin, S. Huang, L. Zhong, S. Wang, D. Han, S. Ren, M. Xiao, Y. Meng, *Energy Storage Mater.* 2021, 34, 128.
- [15] L. Zhou, D. L. Danilov, R.-A. Eichel, P. H. L. Notten, *Adv. Energy Mater.* 2021, 11, 2001304.
- [16] M. Zhao, B.-Q. Li, X.-Q. Zhang, J.-Q. Huang, Q. Zhang, *ACS Cent. Sci.* 2020, 6, 1095.
- [17] Q. Zhang, E. Uchaker, S. L. Candelaria, G. Cao, *Chem. Soc. Rev.* 2013, 42, 3127.
- [18] X. Gu, C. Lai, *Energy Storage Mater.* 2019, 23, 190.
- [19] X. Ji, K. T. Lee, L. F. Nazar, *Nat. Mater.* 2009, 8, 500.
- [20] M. Liu, L. Che, Y. Zhou, N. B. S. Selabi, X. Tian, *Surf. Interfaces* 2024, 53, 105047.
- [21] S. Chen, J. Zhang, Z. Wang, L. Nie, X. Hu, Y. Yu, W. Liu, *Nano Lett.* 2021, 21, 5285.
- [22] Z. W. Seh, Y. Sun, Q. Zhang, Y. Cui, *Chem. Soc. Rev.* 2016, 45, 5605.
- [23] X. Liu, J.-Q. Huang, Q. Zhang, L. Mai, *Adv. Mater.* 2017, 29, 1601759.
- [24] W. Jin, X. Zhang, M. Liu, Y. Zhao, P. Zhang, *Energy Storage Mater.* 2024, 67, 103223.
- [25] K. Zhang, Z. Zhao, H. Chen, Y. Pan, B. Niu, D. Long, Y. Zhang, *Small* 2025, 21, 2409674.
- [26] J. He, A. Manthiram, *Energy Storage Mater.* 2019, 20, 55.
- [27] A. Krause, S. Dörfler, M. Piwko, F. M. Wisser, T. Jaumann, E. Ahrens, L. Giebel, H. Althues, S. Schädlich, J. Grothe, A. Jeffery, M. Grube, J. Brückner, J. Martin, J. Eckert, S. Kaskel, T. Mikolajick, W. M. Weber, *Sci. Rep.* 2016, 6, 27982.
- [28] J. He, A. Manthiram, *Adv. Energy Mater.* 2020, 10, 1903241.
- [29] S. Liu, X. Xia, Y. Zhong, S. Deng, Z. Yao, L. Zhang, X.-B. Cheng, X. Wang, Q. Zhang, J. Tu, *Adv. Energy Mater.* 2018, 8, 1702322.
- [30] C. K. Chan, H. Peng, G. Liu, K. McIlwrath, X. F. Zhang, R. A. Huggins, Y. Cui, *Nat. Nanotechnol.* 2008, 3, 31.
- [31] P. Xue, S. Liu, X. Shi, C. Sun, C. Lai, Y. Zhou, D. Sui, Y. Chen, J. Liang, *Adv. Mater.* 2018, 30, 1804165.
- [32] H. Zhao, N. Deng, J. Yan, W. Kang, J. Ju, Y. Ruan, X. Wang, X. Zhuang, Q. Li, B. Cheng, *Chem. Eng. J.* 2018, 347, 343.
- [33] S. Xia, X. Xu, W. Wu, Y. Chen, L. Liu, G. Wang, L. Fu, Q. Zhang, T. Wang, J. He, Y. Wu, *Mater. Sci. Eng. R: Rep.* 2025, 163, 100924.
- [34] H. Yamin, E. Peled, *J. Power Sources* 1983, 9, 281.
- [35] H. Yamin, A. Goreshtein, J. Penciner, Y. Sternberg, E. Peled, *J. Electrochem. Soc.* 1988, 135, 1045.
- [36] D. Aurbach, E. Pollak, R. Elazari, G. Salitra, C. S. Kelley, J. Affinito, *J. Electrochem. Soc.* 2009, 156, A694.
- [37] Y.-X. Yin, S. Xin, Y.-G. Guo, L.-J. Wan, *Angew. Chem. Int. Ed.* 2013, 52, 13186.
- [38] P. G. Bruce, S. A. Freunberger, L. J. Hardwick, J.-M. Tarascon, *Nat. Mater.* 2012, 11, 19.
- [39] D.-W. Wang, Q. Zeng, G. Zhou, L. Yin, F. Li, H.-M. Cheng, I. R. Gentle, G. Q. M. Lu, *J. Mater. Chem. A* 2013, 1, 9382.
- [40] R. Fang, S. Zhao, Z. Sun, D.-W. Wang, H.-M. Cheng, F. Li, *Adv. Mater.* 2017, 29, 1606823.
- [41] A. Manthiram, Y. Fu, S.-H. Chung, C. Zu, Y.-S. Su, *Chem. Rev.* 2014, 114, 11751.
- [42] Z. Wei, Y. Ren, J. Sokolowski, X. Zhu, G. Wu, *InfoMat* 2020, 2, 483.

- [43] M. R. Busche, P. Adelhelm, H. Sommer, H. Schneider, K. Leitner, J. Janek, *J. Power Sources* **2014**, *259*, 289.
- [44] G. Li, S. Wang, Y. Zhang, M. Li, Z. Chen, J. Lu, *Adv. Mater.* **2018**, *30*, 1705590.
- [45] W. Deng, J. Phung, G. Li, X. Wang, *Nano Energy* **2021**, *82*, 105761.
- [46] G. Zhou, A. Yang, G. Gao, X. Yu, J. Xu, C. Liu, Y. Ye, A. Pei, Y. Wu, Y. Peng, Y. Li, Z. Liang, K. Liu, L.-W. Wang, Y. Cui, *Sci. Adv.* **2020**, *6*, eaay5098.
- [47] M. Wild, L. O'Neill, T. Zhang, R. Purkayastha, G. Minton, M. Marinescu, G. J. Offer, *Energy Environ. Sci.* **2015**, *8*, 3477.
- [48] D. Luo, G. Li, Y.-P. Deng, Z. Zhang, J. Li, R. Liang, M. Li, Y. Jiang, W. Zhang, Y. Liu, W. Lei, A. Yu, Z. Chen, *Adv. Energy Mater.* **2019**, *9*, 1900228.
- [49] G. Zhou, L. Xu, G. Hu, L. Mai, Y. Cui, *Chem. Rev.* **2019**, *119*, 11042.
- [50] K. Yu, X. Pan, G. Zhang, X. Liao, X. Zhou, M. Yan, L. Xu, L. Mai, *Adv. Energy Mater.* **2018**, *8*, 1802369.
- [51] H. Zhang, H. Xu, Z. Xiao, G. Dong, Y. Cheng, F. Fei, X. Hu, L. Xu, L. Mai, *Adv. Funct. Mater.* **2025**, *35*, 2412548.
- [52] L. Djuandhi, U. Mittal, N. Sharma, H. L. Andersen, *J. Electrochem. Soc.* **2023**, *170*, 010522.
- [53] N. B. S. Selabi, Y. Zhou, L. Che, M. Liu, L. Mo, L. D. W. Djouonke, X. Tian, *J. Power Sources* **2025**, *626*, 235785.
- [54] N. B. S. Selabi, Y. Zhou, L. Che, M. Liu, L. Mo, X. Tian, *Chem. Eng. J.* **2025**, *504*, 157724.
- [55] L. Ni, S. Duan, H. Zhang, J. Gu, G. Zhao, Z. Lv, G. Yang, Z. Ma, Y. Liu, Y. Fu, Z. Wu, J. Xie, M. Chen, G. Diao, *Carbon* **2021**, *182*, 335.
- [56] T. Wang, X. Zhang, J. Yang, J. Cui, J. Yan, J. Liu, Y. Wu, *Nanoscale Adv.* **2025**, *7*, 506.
- [57] M. Xiang, H. Zhang, S. Feng, J. Xiao, X. Li, *J. Electroanal. Chem.* **2021**, *900*, 115721.
- [58] J. Lee, T. Hwang, Y. Lee, J. K. Lee, W. Choi, *Mater. Lett.* **2015**, *158*, 132.
- [59] Q. Li, Z. Ma, J. Zhao, K. Shen, T. Shi, Y. Xie, Y. Fan, X. Qin, G. Shao, *J. Power Sources* **2022**, *521*, 230929.
- [60] X. Wang, Z. Sun, Y. Zhao, J. Li, Y. Zhang, Z. Zhang, *J. Solid State Electrochem.* **2020**, *24*, 111.
- [61] S. Zhao, Y. Li, F. Zhang, J. Guo, *J. Alloys Compd.* **2019**, *805*, 873.
- [62] J. Jin, J. Cai, X. Wang, Z. Sun, Y. Song, J. Sun, *FlatChem* **2021**, *27*, 100236.
- [63] Y. Cai, Z. Yan, S. Shi, L. Zhang, T. Zhang, M. Yang, L. Bai, H. Fu, X.-S. Yang, Z. Li, Z.-D. Huang, *Scr. Mater.* **2021**, *202*, 113989.
- [64] Y. Yan, T. Lei, Y. Jiao, C. Wu, J. Xiong, *Electrochim. Acta* **2018**, *264*, 20.
- [65] C. Zha, D. Wu, T. Zhang, J. Wu, H. Chen, *Energy Storage Mater.* **2019**, *17*, 118.
- [66] Y. X. Ren, T. S. Zhao, M. Liu, L. Wei, R. H. Zhang, *Electrochim. Acta* **2017**, *242*, 137.
- [67] G. Zhou, Y. Zhao, C. Zu, A. Manthiram, *Nano Energy* **2015**, *12*, 240.
- [68] P.-W. Chen, C.-C. Cheng, Y.-C. Ting, T.-Y. Lin, F.-Y. Yen, G.-R. Li, S.-Y. Lu, *J. Taiwan Inst. Chem. Eng.* **2024**, *164*, 105699.
- [69] C. Zha, D. Wu, X. Gu, H. Chen, *J. Energy Chem.* **2021**, *59*, 599.
- [70] G. Gourdin, S. Mendez, V. Doan-Nguyen, *ACS Appl. Mater. Interfaces* **2023**, *15*, 55596.
- [71] Y. Qiu, X.-J. Yin, M.-X. Wang, M. Li, X. Sun, B. Jiang, H. Zhou, D.-Y. Tang, Y. Zhang, L.-S. Fan, N.-Q. Zhang, *Rare Met.* **2021**, *40*, 3147.
- [72] G. Li, J. Li, K. Wang, J. Zhang, K. Liao, H. Zhang, *ACS Appl. Mater. Interfaces* **2024**, *16*, 35123.
- [73] Z. Wang, J. Shen, J. Liu, X. Xu, Z. Liu, R. Hu, L. Yang, Y. Feng, J. Liu, Z. Shi, L. Ouyang, Y. Yu, M. Zhu, *Adv. Mater.* **2019**, *31*, 1902228.
- [74] J. Shen, X. Xu, J. Liu, Z. Liu, F. Li, R. Hu, J. Liu, X. Hou, Y. Feng, Y. Yu, M. Zhu, *ACS Nano* **2019**, *13*, 8986.
- [75] J. Zhou, X. Liu, L. Zhu, J. Zhou, Y. Guan, L. Chen, S. Niu, J. Cai, D. Sun, Y. Zhu, J. Du, G. Wang, Y. Qian, *Joule* **2018**, *2*, 2681.
- [76] H. Yuan, X. Chen, G. Zhou, W. Zhang, J. Luo, H. Huang, Y. Gan, C. Liang, Y. Xia, J. Zhang, J. Wang, X. Tao, *ACS Energy Lett.* **2017**, *2*, 1711.
- [77] J. Li, W. Xie, S. Zhang, S.-M. Xu, M. Shao, *J. Mater. Chem. A* **2021**, *9*, 11151.
- [78] Z. Shen, M. Cao, Z. Zhang, J. Pu, C. Zhong, J. Li, H. Ma, F. Li, J. Zhu, F. Pan, H. Zhang, *Adv. Funct. Mater.* **2020**, *30*, 1906661.
- [79] D.-R. Deng, F. Xue, Y.-J. Jia, J.-C. Ye, C.-D. Bai, M.-S. Zheng, Q.-F. Dong, *ACS Nano* **2017**, *11*, 6031.
- [80] Z. Sun, J. Zhang, L. Yin, G. Hu, R. Fang, H.-M. Cheng, F. Li, *Nat. Commun.* **2017**, *8*, 14627.
- [81] Z. Cui, C. Zu, W. Zhou, A. Manthiram, J. B. Goodenough, *Adv. Mater.* **2016**, *28*, 6926.
- [82] Z. Li, Q. He, X. Xu, Y. Zhao, X. Liu, C. Zhou, D. Ai, L. Xia, L. Mai, *Adv. Mater.* **2018**, *30*, 1804089.
- [83] C. Zha, X. Zhu, J. Deng, Y. Zhou, Y. Li, J. Chen, P. Ding, Y. Hu, Y. Li, H. Chen, *Energy Storage Mater.* **2020**, *26*, 40.
- [84] X. Xiao, X. Peng, H. Jin, T. Li, C. Zhang, B. Gao, B. Hu, K. Huo, J. Zhou, *Adv. Mater.* **2013**, *25*, 5091.
- [85] X. Li, K. Ding, B. Gao, Q. Li, Y. Li, J. Fu, X. Zhang, P. K. Chu, K. Huo, *Nano Energy* **2017**, *40*, 655.
- [86] B. Fei, C. Zhang, D. Cai, J. Zheng, Q. Chen, Y. Xie, L. Zhu, A. Cabot, H. Zhan, *ACS Nano* **2021**, *15*, 6849.
- [87] J. Pu, W. Gong, Z. Shen, L. Wang, Y. Yao, G. Hong, *Adv. Sci.* **2022**, *9*, 2104375.
- [88] H. Zhang, L. Wang, Q. Li, L. Ma, T. Wu, Y. Ma, J. Wang, C. Du, G. Yin, P. Zuo, *Carbon* **2018**, *140*, 385.
- [89] S. Davood, M. Morteza, B. Majid, *Solid State Ion.* **2022**, *382*, 115958.
- [90] L. Luo, S.-H. Chung, H. Y. Asl, A. Manthiram, *Adv. Mater.* **2018**, *30*, 1804149.
- [91] Z. Song, W. Jiang, B. Li, Y. Qu, R. Mao, X. Jian, F. Hu, *Small* **2024**, *20*, 2308550.
- [92] K. Zhang, J. Li, Q. Li, J. Fang, Z. Zhang, Y. Lai, Y. Tian, *Appl. Surf. Sci.* **2013**, *285*, 900.
- [93] J. Liu, M. Cheng, T. Han, Y. Chen, J. Long, X. Zeng, L. Cheng, Z. Peng, P. Zhou, *J. Electroanal. Chem.* **2019**, *855*, 113543.
- [94] X. Yang, Z. Tang, R. Liao, J. Zhou, Y. Pan, P. Gao, G. Li, L. Yu, F. Wu, *J. Power Sources* **2024**, *602*, 234315.
- [95] B. Liu, J. Wang, Z. Li, Z. Sun, C. Li, J.-M. Seo, J. Li, Y. Guo, H. Yao, S. Guan, J.-B. Baek, *Nano Energy* **2024**, *126*, 109611.
- [96] H. Yu, A. Siebert, S. Mei, R. Garcia-Diez, R. Félix, T. Quan, Y. Xu, J. Frisch, R. G. Wilks, M. Bär, C. Pei, Y. Lu, *Energy Environ. Mater.* **2024**, *7*, e12539.
- [97] Y. Xiao, S. Guo, Y. Xiang, D. Li, C. Zheng, Y. Ouyang, A. Cherevan, L. Gan, D. Eder, Q. Zhang, S. Huang, *ACS Energy Lett.* **2023**, *8*, 5107.
- [98] D. Zhu, T. Long, B. Xu, Y. Zhao, H. Hong, R. Liu, F. Meng, J. Liu, *J. Energy Chem.* **2021**, *57*, 41.
- [99] H.-Y. Choi, S.-H. Lee, H.-J. Yu, S.-H. Yu, *Bull. Korean Chem. Soc.* **2024**, *45*, 382.
- [100] S. Xia, Z. Chen, L. Yuan, J. Song, Q. Zhou, X. Yuan, L. Liu, L. Fu, Y. Chen, Y. Wu, *J. Mater. Chem. A* **2023**, *11*, 19870.
- [101] S. Xia, J. Song, Q. Zhou, L. Liu, J. Ye, T. Wang, Y. Chen, Y. Liu, Y. Wu, T. van Ree, *Adv. Sci.* **2023**, *10*, 2301386.
- [102] Y. Wang, W. Liu, R. Liu, P. Pan, L. Suo, J. Chen, X. Feng, X. Wang, Y. Ma, W. Huang, *New J. Chem.* **2019**, *43*, 14708.
- [103] K. Chen, G. Zhang, L. Xiao, P. Li, W. Li, Q. Xu, J. Xu, *Small Methods* **2021**, *5*, 2001056.
- [104] X. Zhou, Q. Liao, J. Tang, T. Bai, F. Chen, J. Yang, *J. Electroanal. Chem.* **2016**, *768*, 55.
- [105] X. Yu, N. Wang, Z. Sun, L. Shao, X. Shi, J. Cai, *Electrochim. Acta* **2023**, *457*, 142497.
- [106] Z.-D. Huang, M.-T. Yang, J.-Q. Qi, P. Zhang, L. Lei, Q.-C. Du, L. Bai, H. Fu, X.-S. Yang, R.-Q. Liu, T. Masese, H. Zhang, Y.-W. Ma, *Chem. Eng. J.* **2020**, *387*, 124080.
- [107] G. H. Park, W.-G. Lim, Y. H. Jeong, S. K. Kang, M. Kim, J. Ji, J. Ha, S. R. Mangisetti, S. Kim, Y. Park, C. Jo, W. B. Kim, *Small Struct.* **2024**, *5*, 2400293.
- [108] L. Zhang, X. Chen, F. Wan, Z. Niu, Y. Wang, Q. Zhang, J. Chen, *ACS Nano* **2018**, *12*, 9578.
- [109] J. Guo, H. Pei, Y. Dou, S. Zhao, G. Shao, J. Liu, *Adv. Funct. Mater.* **2021**, *31*, 2010499.
- [110] X. Yu, Y. Yin, C. Ma, J. Xu, W. Qiao, J. Wang, L. Ling, *Chem. Eng. Sci.* **2023**, *268*, 118400.
- [111] T. Zhao, Y. Ye, X. Peng, G. Divitini, H.-K. Kim, C.-Y. Lao, P. R. Coxon, K. Xi, Y. Liu, C. Ducati, R. Chen, R. V. Kumar, *Adv. Funct. Mater.* **2016**, *26*, 8418.
- [112] S.-K. Lee, H. Kim, S. Bang, S.-T. Myung, Y.-K. Sun, *Molecules* **2021**, *26*, 377.
- [113] H. Ahn, Y. Kim, J. Bae, Y. K. Kim, W. B. Kim, *Chem. Eng. J.* **2020**, *401*, 126042.
- [114] Y. Guo, Y. Zhang, Y. Zhang, M. Xiang, H. Wu, H. Liu, S. Dou, *J. Mater. Chem. A* **2018**, *6*, 19358.
- [115] P. Wang, Z. Zhang, B. Hong, K. Zhang, J. Li, Y. Lai, *J. Electroanal. Chem.* **2019**, *832*, 475.
- [116] J. Zhao, Y. Zhao, W.-c. Yue, X. Li, N. Gao, Y.-j. Zhang, C.-q. Hu, *Chem. Eng. J.* **2022**, *441*, 136082.
- [117] Y. Kim, Y. Noh, J. Bae, H. Ahn, M. Kim, W. B. Kim, *J. Energy Chem.* **2021**, *57*, 10.
- [118] D. W. Kim, C. Senthil, S. M. Jung, S.-S. Kim, H.-S. Kim, J. W. Hong, J.-H. Ahn, H. Y. Jung, *Energy Storage Mater.* **2022**, *47*, 472.
- [119] S. Zhang, H. Shi, J. Tang, W. Shi, Z.-S. Wu, X. Wang, *Sci. China Mater.* **2021**, *64*, 2949.
- [120] R. Li, X. Sun, J. Zou, Q. He, *J. Electroanal. Chem.* **2020**, *856*, 113662.

- [121] W. Yan, X. Gao, J.-L. Yang, X. Xiong, S. Xia, W. Huang, Y. Chen, L. Fu, Y. Zhu, Y. Wu, *Small* **2022**, *18*, 2106679.
- [122] J. Shen, Z. Wang, X. Xu, Z. Liu, D. Zhang, F. Li, Y. Li, L. Zeng, J. Liu, *Adv. Energy Sustain. Res.* **2021**, *2*, 2100007.
- [123] Q. Liang, S. Wang, Y. Yao, P. Dong, H. Song, *Adv. Funct. Mater.* **2023**, *33*, 2300825.
- [124] S. Feng, Z.-H. Fu, X. Chen, Q. Zhang, *InfoMat* **2022**, *4*, e12304.
- [125] J. Li, Y. Chen, S. Zhang, W. Xie, S.-M. Xu, G. Wang, M. Shao, *ACS Appl. Mater. Interfaces* **2020**, *12*, 49519.
- [126] M. Majid, Z. Deng, X. Wang, *Nano Energy* **2024**, *132*, 110387.
- [127] L. Chen, G. Cao, Y. Li, G. Zu, R. Duan, Y. Bai, K. Xue, Y. Fu, Y. Xu, J. Wang, X. Li, *Nano-Micro Lett.* **2024**, *16*, 97.
- [128] Q. Gu, M. Lu, Y. Cao, B. Zhang, *Renewables* **2023**, *1*, 601.
- [129] S. Rehman, M. Pope, S. Tao, E. McCalla, *Energy Environ. Sci.* **2022**, *15*, 1423.
- [130] M. Hagen, P. Schiffels, M. Hammer, S. Dörfler, J. Tübke, M. J. Hoffmann, H. Althues, S. Kaskel, *J. Electrochem. Soc.* **2013**, *160*, A1205.
- [131] M. U. M. Patel, R. Demir-Cakan, M. Morcrette, J.-M. Tarascon, M. Gaberscek, R. Dominko, *ChemSusChem* **2013**, *6*, 1177.
- [132] G. F. Hawes, C. Punckt, M. A. Pope, *ACS Appl. Mater. Interfaces* **2021**, *13*, 31569.
- [133] Z. Wang, Y. Tang, X. Fu, J. Wang, Z. Peng, L. Zhang, J. Huang, *ACS Appl. Mater. Interfaces* **2020**, *12*, 55971.
- [134] K. Shi, Z. Sui, X. Xu, J. Qiu, Q. Chen, Q. Song, Z. Sui, *J. Mater. Sci.* **2024**, *59*, 3947.
- [135] G. Ma, F. Huang, Z. Wen, Q. Wang, X. Hong, J. Jin, X. Wu, *J. Mater. Chem. A* **2016**, *4*, 16968.

Manuscript received: July 11, 2025

Revised manuscript received: August 25, 2025

Version of record online: